Advanced Microstructure Optimization Strategies for High-Temperature CO_2 Electrolysis: Infiltration and In-situ Exsolution

by
Shaochen Ding

A thesis submitted in partial fulfillment of the requirements for the degree of

Master of Science

In

Chemical Engineering

Department of Chemical and Materials Engineering
University of Alberta

©Shaochen Ding, 2019

Abstract

The solid oxide electrolysis cell (SOEC) has attracted increased attention in recent years due to its capability to reduce CO_2 emissions in a highly efficient and environmentally sustainable fashion. Previous work in our group has fabricated an A-site Ce doped $La_{0.7}Sr_{0.3}Cr_{0.5}Fe_{0.5}O_{3-\delta}$ (LSCeCrF) with gadolinium doped ceria (GDC) as the cathode material in SOEC by the conventional method. This material presents a satisfying electrochemical performance and good stability due to the presence of excessive oxygen vacancies, which constitute the strong CO_2 adsorption ability of the material. However, the electrochemical catalytic activity is still limited by the catalyst specific area. Hence, the optimization of electrode microstructure is considered as a promising way to further improve the SOEC performance by increasing the active reaction area.

In this thesis, LSCeCrF and GDC composite cathode was firstly fabricated by infiltration method, and the results were compared with one from our previous study with a conventional fabrication method. From analysis of laboratory results, it is evident that the infiltration method can effectively improve electrochemical performance of SOEC, with optimized microstructure of the cathode. Secondly, to further improve the catalytic activity for CO_2 conversion, $(La_{0.65}Sr_{0.3}Ce_{0.05})_{0.9}(Cr_{0.5}Fe_{0.5})_{0.85}Ni_{0.15}O_{3-\delta}$ (Ni-LSCeCrF)/GDC nanostructured cathode was fabricated by infiltration and in situ exsolution of highly active Ni-Fe alloy nanoparticles.

The effects of electrode microstructure optimization on the electrochemical performance were investigated in the atmospheres of pure CO_2, and mixture of CO_2 and CO (CO_2 mole fraction as 0.7). The Ni-LSCeCrF/GDC cathode shows significantly improved electrochemical performance, CO production rate, and Faraday efficiency for CO_2 reduction in both atmospheres. Furthermore, collaboration with Ms. Wanying Pang, PhD student supervised by Professor Zhehui

Jin, density function theory calculations were carried out to investigate the exsolution trends of transition metals on B-site of a perovskite lattice. The results show that Ni doping could reduce the segregation energy of Fe, revealing an alternative strategy of multiple elements doping to form active alloy by in situ exsolution.

Preface

The main results in Chapter 3 and Chapter 4 of this thesis have been submitted to *Electrochimica Acta* (under review after first revision) as Shaochen Ding, Dr. Meng Li, Wanying Pang, Dr. Bin Hua, Dr. Nanqi Duan, Dr. Yaqian Zhang, Shengnian Zhang, Dr. Zhehui Jin, Dr. Jingli Luo. "A-site deficient with nano-socket Ni-Fe alloy particles as highly active and durable catalyst for high-temperature CO_2 electrolysis". The author has led the data collection and analysis, and the manuscript composition of the report. Dr. Meng Li contributed to the experimental procedure teaching and manuscript editing. Wanying Pang contributed to the density function theory (DFT) calculations. Dr. Bin Hua and Dr. Nanqi Duan contributed to concept formation and experiment design. Dr. Yaqian Zhang and Shengnian Zhang contributed to electron microscopy data collection. Dr. Zhenghui Jin and Dr. Jingli Luo were the supervisory authors.

Acknowledgement

I would like to give my most sincere appreciation to my dear supervisor, Dr. Jingli Luo for all the guidance and encouragement from her. It was her great patience and understandings that encouraged and pacified me when I struggled with problems and troubles. The knowledge and ideas I have received from her not only helped me to accomplish my research in the past two years but also opened up my eyes to a wider vision of the world. I am so proud to be one of her students.

My deep appreciation also goes to Dr. Bin Hua and Dr. Meng Li for their valuable advice and suggestive discussions with me throughout the process of my research. Their dedication and broad knowledge inspired and motivated me, making my two years of study an extremely valuable and unforgettable experience.

I am grateful to Wanying Pang, and her supervisor Zhehui Jin with their help on the density function theory calculations. I also wish to thank my colleagues and friends, Dr. Nanqi Duan, Dr. Yaqian Zhang, Shengnian Zhang, Zhou Chen for all their support, help and encouragement during my stay at the University of Alberta.

This work is supported by Alberta Innovates Technology Futures fund, and the Discovery Grant from the Natural Sciences and Engineering Research Council of Canada. This research was enabled in part by support provided by Westgrid (www.westgrid.ca) and Compute Canada (www.computecanada.ca). As a part of the University of Alberta's Future Energy Systems research initiative, this research was made possible in part thanks to funding from the Canada First Research Excellence Fund.

Table of Contents

List of Figures

List of Symbols

θ	Angle of Incidence
d	Distance
λ	Wavelength
E_f	Oxygen Vacancy Formation Energy
E_{o2}	Total Energy of One Oxygen Molecule in the isolated gas phase
E_{o_v}	Total Energy of the slab with Oxygen Vacancy
E_{clean}	Total Energy of the slab without Oxygen Vacancy
E_{ex}	Co-segregation Energy
$E_{B\text{-}Ov\_surf}$	Energy of after B-site metal and the oxygen vacancy segregation
$E_{B\text{-}Ov\_bulk}$	Energy of before B-site metal and the oxygen vacancy segregation

List of Abbreviations

SOEC	Solid Oxide Electrolysis Cell
PEMEC	Polymer Electrolyte Membrane Electrolysis Cell
SOFC	Solid Oxide Fuel Cell
CO_2	Carbon Dioxide
CO	Carbon Monoxide
O	Oxygen
Fe	Iron
Ni	Nickel
La	Lanthanum
Sr	Strontium
Ce	Cerium
Cr	Chromium
Co	Cobalt
G	Gallium
Ce	Cerium
Gd	Gadolinium
Sc	Scandia
Zr	Zirconium
S	Samarium
Mn	Manganese
Mg	Magnesium

Ti	Titanium
Y	Yttria
LSCeCrF	$La_{0.65}Sr_{0.3}Ce_{0.05}Cr_{0.5}Fe_{0.5}$
GDC	$Gd_{0.1}Ce_{0.9}O_{1.95}$
Ni-LSCeCrF	$(La_{0.65}Sr_{0.3}Ce_{0.05})_{0.9}(Cr_{0.5}Fe_{0.5})_{0.85}Ni_{0.15}O_{3-\delta}$
LSCF	$La_{0.6}Sr_{0.4}Co_{0.2}Fe_{0.8}O_{3-\delta}$
YSZ	Yttria-stabilized Zirconia
ScSz	Scandia stabilized zirconia
SDC	Samarium-doped ceria
LSGMg	Lanthanum Strontium Gallium Magnesium
LSCM	Lanthanum Strontium Chromate Manganese
LSM	Lanthanum Strontium Manganese
LSTC	Chromite doped Lanthanum Strontium Titanium
LSTM	Manganese doped Lanthanum Strontium Titanium
LSCrX	Lanthanum Strontium Chromate-based Perovskite
GHG	Greenhouse Gas
IC	Ionic Conductivity
EC	Electronic Conductivity
MIEC	Mixed Ionic and Electronic Conductivity
TPB	Triple Phase Boundary
OCV	Open Circuit Voltage
NP	Nanoparticles
OER	Oxygen Evolution Reaction

ASR	Area Specific Resistance
PD-GNP	Particle-dispersed Glycine Nitrate Process
TPD	Temperature Programmed Desorption
DFT	Density Function Theory
GC	Gas Chromatography
EIS	Electrochemical Impedance Spectra
R_s	Ohmic Resistance
R_p	Polarization Resistance
R_H	High Frequency Polarization Resistance
R_L	Low Frequency Polarization Resistance
AC	Alternative Current
XRD	X-ray Diffraction
STEM	Scanning Transmission Electron Microscope
EDX	Energy Dispersive X-ray Spectroscopy
FESEM	Field Emission Scanning Electron Microscope
HAADF	High-angle Annular Dark Field
VASP	Vienna ab initio Simulation Package
LCFO	$LCr_{0.5}Fe_{0.5}O_3$
Perdew-Burke-Ernzerhof	PBE
GGA	Generalized Gradient Approximation
PAW	Projector Augmented Wave
LSFNO	Ni-doped LCFO

Chapter 1 Introduction

1.1 Global CO_2 Emission Problem

In recent decades, the unparalleled speed of inventions of new technology by human society resulted in a dramatic increase in energy consumption that mainly relies on the combustion of fossil fuels [1]. The heavy dependence on fossil fuels leads to a large amount of greenhouse gas (GHG), mostly carbon dioxide (CO_2), emissions. Figure 1.1 shows the global CO_2 emissions trend, from the beginning of the last century, 1900, until 2014 [2]. The CO_2 emissions are estimated from the combustion of fossil fuels (solid, liquid, and gas fuel sources), and industrial processes, including cement production and gas flaring. It is seen that from 1970, the CO_2 emissions have been increased by about 90%, which account for about 78% of total GHG emission increase [3].

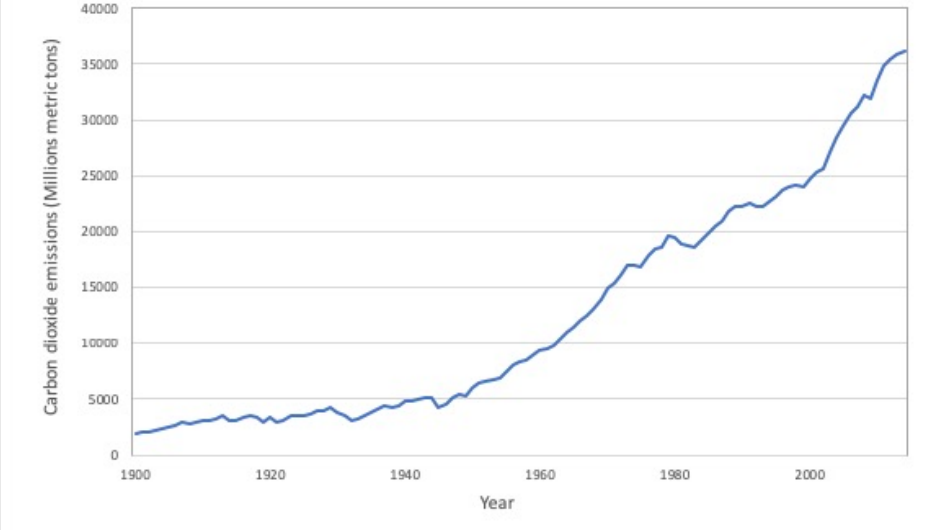

Figure 1.1 Global CO_2 Emission from Fossil Fuel Consumption and Industrial Processes [2]

Due to the large amount of CO_2 emission, the global atmospheric CO_2 concentration has experienced a dramatic rise most recently. Figure 1.2 shows the actual atmospheric CO_2 concentration from 1986 to 2007 measured from the monitoring site at Alert, NWT, Canada. It can be seen in that period of about 20 years, the global atmospheric CO_2 concentration has been increased from 4200 ppmv to above 4600 ppmv, and the annual average value rose from 348.48 ppmv to 384.84 ppmv [4]. Although CO_2 is a crucial ingredient for the life cycle of animals and plants and is very important in the carbon cycle of the earth, the increased atmospheric CO_2 caused unexpected climate change and severe environmental destroy, such as global warming. Therefore, a feasible solution to reduce CO_2 emission and convert it into useful industrial materials without causing further pollution, becomes extremely attractive [5].

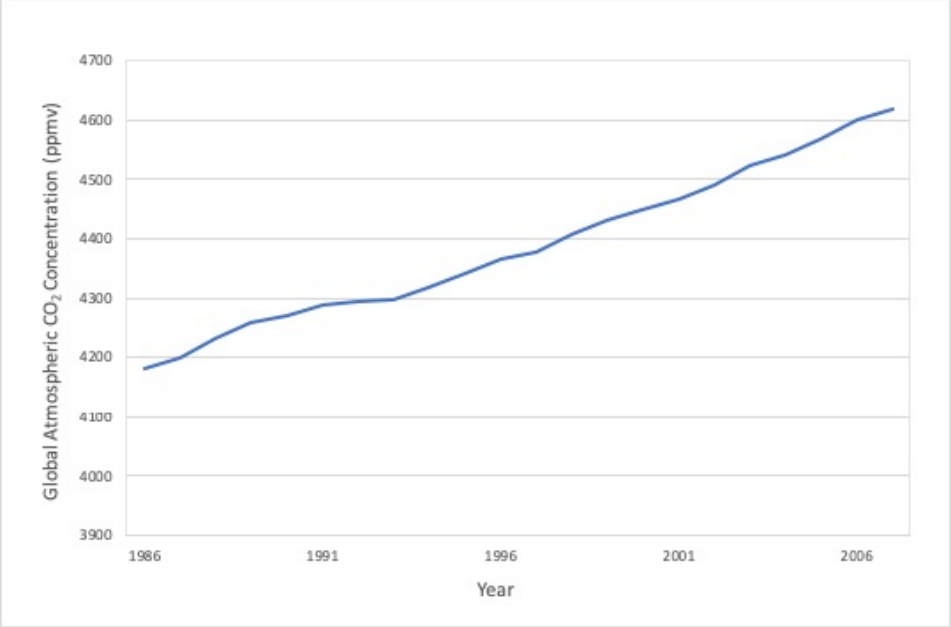

Figure 1.2. Global Atmospheric CO_2 Concentration From 1986 to 2007 measured from Albert, NWT, Canada [4].

1.2 Alternatives for CO_2 Utilization

There are two main categories for technological utilization of CO_2: one is non-reductive and the other one is reductive. For the non-reductive utilization process, CO_2 will keep quadrivalent state, which requires only slight energy exchange. The products are mostly chemicals such as inorganic and organic carbonates, urea, organic carbamates, and carboxylic acids. Regarding the reductive process, CO_2 will experience oxidative conversion to a lower state, in which the procedure requires high energy consumption. The typical products include methane, ethylene, methanol, ethanol, formic acid, and carbon monoxide [6]. Although the second process needs strong reducing reagents, associated with the requirement of electricity, heat, radiation, and catalyst in most cases, it is still much more attractive considering economically and environmentally as the products of CO_2 reduction from this process can be used as fuel, based on the fact of larger global fuel market compared with chemical market [7].

Under the category of reductive utilization, there are typically three methods: photocatalysis, thermocatalysis, and electrochemical catalysis [8]. For photocatalysis, electrons and holes are firstly generated when light (photon) is absorbed by semiconductor materials. Then the photogenerated electron-hole pairs are separated and transported to active catalytic sites on the semiconductor surface. At the catalyst surface, electrons are used to reduce CO_2 to hydrocarbon fuels while holes oxidize H_2O to O_2 [9]. For the thermocatalytic process, the catalyst is activated by thermal energy, and promotes H_2O vapor and CO_2 molecules to be re-oxidized and reorganized into fuels [10]. In the case of electrochemical catalysis, electrons are generated when there is an applied potential across two electrodes. The electrons are combined with CO_2 to convert into CO and other hydrocarbons on the cathode while O_2 evolution occurs on the anode [11].

Among these technological CO_2 reductive utilization, the electrochemical catalysis with electrolysis cell is more attractive due to the following advantages: the reaction system is highly efficient, compact and scaled, and the process is easy to be controlled by modifying electrode potentials and reaction temperatures; the production of hydrocarbons from electricity, CO_2, and water is able to direct applied as transportation fuel; and the process heat inputs can be supplied from clean and renewable energy sources [12].

1.3 Solid Oxide Electrolysis Cell (SOEC)

The electrolysis cell is established based on the concept of fuel cells, with similar components in essence: two electrodes and an electrolyte. The role of electrolyte is to transfer oxygen ions from one electrode to the other, and the material for electrolyte must be electron insulating. The cathode, also known as fuel electrode, is where reduction of reactants happens. The oxidation occurs at the anode that is also called the air electrode. Half-cell reaction takes place at each electrode, which constitute the overall electrochemical reaction.

According to the electrolyte materials, the electrolysis cells can be divided into several different types that are suitable for using at various operation temperatures and purposes. Liquid alkaline and acid solution can be used as the electrolyte material. The electrolysis cells using these two kinds of materials are usually operated at low temperature and are more capable of water electrolysis. The disadvantages are low efficiency and selectivity, low electrode durability, and expensive electrode materials. Some solid materials can also be used as the electrolyte, such as polymer and some ceramics. The polymer electrolyte membrane electrolysis cell (PEMEC) is a commercially available low operation temperature device, and commonly used for electrolyzing water. The electrode of PEMEC is made of noble metals, carrying a relatively high fabrication

cost; also, at elevated temperature, the hydrogen crossover through the membrane will increase. Solid oxide electrolysis cell (SOEC) uses solid ceramic as electrolyte material to transfer oxygen ions and attracts much attention recently. SOEC is able to electrolyze H_2O and/or CO_2 at high operation temperature (600 °C-1000°C) [13, 14].

Solid oxide electrolysis cell (SOEC) is a promising high operation temperature system where CO_2 can be converted into carbon monoxide (CO) under external applied potential with its advantages of environmental friendliness and high efficiency [13]. SOEC is conceptually a solid oxide fuel cell (SOFC) operating in reverse. The discovery of solid oxide electrolytes in 1899 by Nernst proposed the idea of SOFC first [15]. In 1935, Schottky mentioned the yttria-stabilized zirconia (YSZ) as the solid oxide electrolyte, leading to the fast development of SOFC [16]. The schematic diagram of the structure and operational principle of SOFC is shown in Figure 1.3. SOFCs are complicated electrochemical devices containing three fundamental components: the porous anode, the porous cathode, and the dense electrolyte. The dense solid electrolyte can be regarded as the separator of air and fuel, and the oxygen ion conductor. The electrodes are the interface between chemical, electrical energy, and catalyst for fuel oxidation. Oxygen (O_2) is supplied on one side of the SOFC, and carbon monoxide is provided from the other side. O_2 is reduced to oxygen ions at the cathode. Then oxygen ions can transfer through the solid electrolyte to the anode. Fuel source in this case, the carbon monoxide molecules, are able to react with the oxygen ions at the anode producing CO_2 with electricity and heat. SOFCs can reach a theoretical maximum efficiency of about 80%, in an elevated operation temperature of 500-1000^{o}C [17].

Many researchers have found that the SOFC can be used as an electrolysis cell as well with applied voltages. SOEC has the same structure as SOFC but with some electrode material limitations. SOEC with nickel ceramic or platinum electrode was first applied by NASA to

generate O_2 using CO_2 as the feed gas, and then it was widely studied to produce fuels [14]. The schematic diagram for the SOEC is also shown in Figure 1.3. Compared with SOFC, CO_2 can be electrochemically converted to CO fuel and oxygen ions at cathode, and the oxygen ions at anode that are transported through electrolyte from cathode can be oxidized to O_2. It has the advantages of high efficiency, low-cost electrolyte and electrode material, and good durability. Also, the high operation temperature enables lower electricity consumption, with heating sources easily obtainable from industrial waste heat or renewable heat resources, which further reduce the operation cost [13, 14]. In SOEC, in order to better reduce CO_2 and obtain high active catalytic efficiency, the porosity and microstructure of electrodes to increase the catalyst specific area are key aspects that have to be considered. The intrinsic catalytic activity is required to be raised above certain minimum thresholds, in order to initialize the reaction. Also, the ionic conductivity (IC) to transfer charging carriers and electronic conductivity (EC) to provide paths for electrons are necessary properties for the electrode materials. The three characters mentioned above are key parameters to be satisfied for the electrode performance, with any deficiencies leading to significant drop of SOEC performance. Overall, a porous electrode to ensure satisfying gas diffusion and a good contact interface between gas, EC, and IC, known as the triple phase boundary (TPB), often requires high number of active reaction sites to enable satisfactory reaction rates of CO_2 reduction [18].

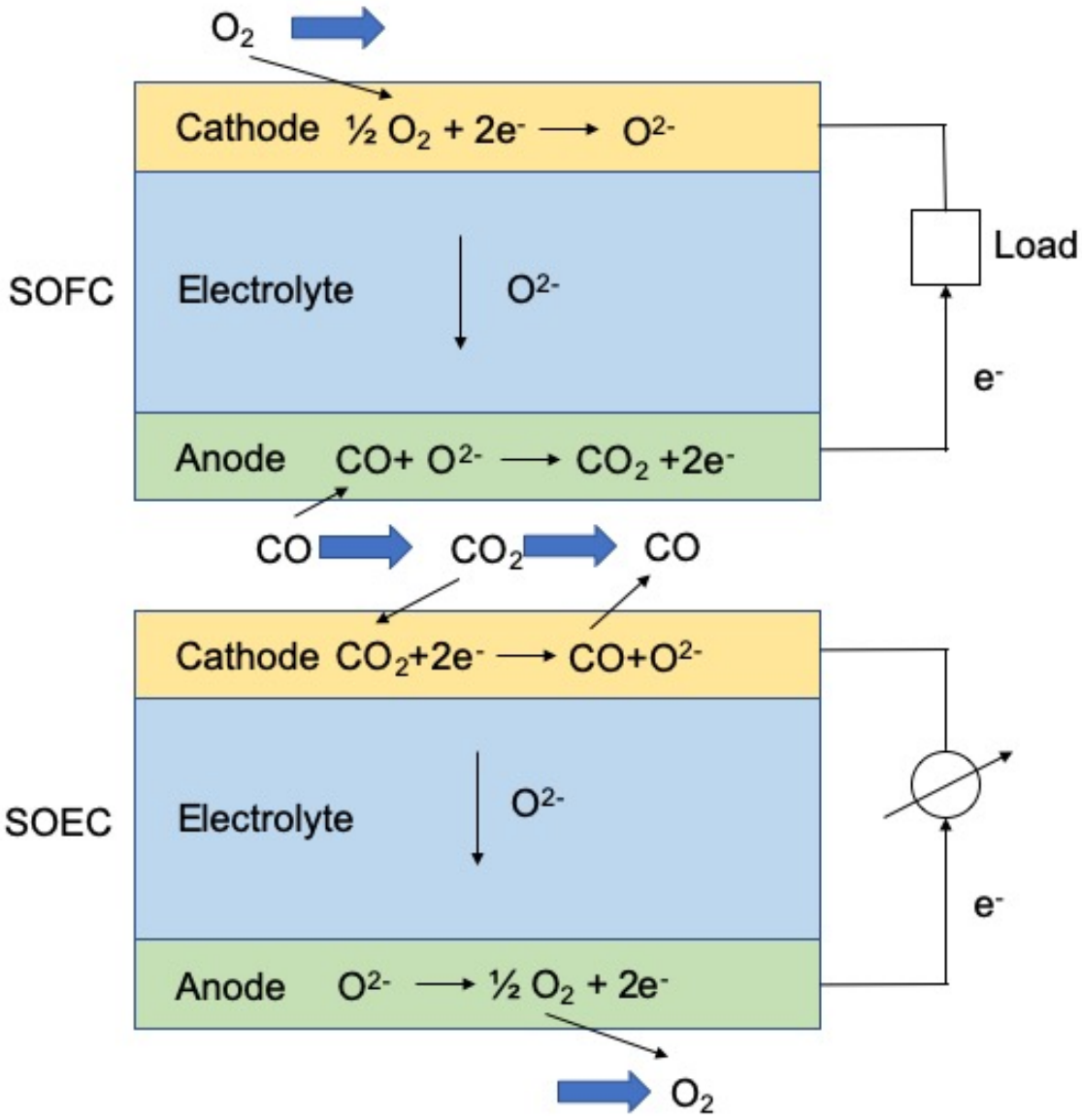

Figure 1.3. Schematic Diagram of structure and operational principle for SOFC and SOEC.

Traditionally, the SOEC is electrolyte supported, which means that it has a dense and thick electrolyte layer with electrodes fabricated on it. The electrolyte using well-studied material such as YSZ and gadolinium doped ceria (GDC) with a thickness of 100 μm-300 μm is already commercialized. However, the thick electrolyte layer will bring high ohmic intrinsic resistance and ionic losses. Recently, there is a newly researched and fast developing SOEC geometry, called

cathode supported structure. In the cathode supported geometry, a thick porous Ni-YSZ substrate is treated as support layer, and there is a functional layer containing catalyst for CO_2 reduction and a thin YSZ electrolyte fabricating on it. It has advantages of increased ionic conductivity and mechanical strength, leading to improved electrochemical performance and durable structure under long term operation [19].

Through the integrated system of SOFC and SOEC, the electricity can be generated by SOFC and the CO_2 produced from SOFC can be fed into SOEC as the fuel to reduce CO_2 emission. After the reaction in SOEC, the product CO can be used as fuel of SOFC again. The process itself is able to close the carbon cycle as shown in Figure 1.4. Closing carbon cycle means that the CO_2 emission and utilization can be combined through CO_2 capture, and the products from CO_2 utilization can be reused [20]. There is also another design which is called reversible SOFC (SOEC) [21-23]. This design of reversible cell can combine the fuel utilization and CO_2 utilization in one device to achieve the goal of closing carbon cycle better.

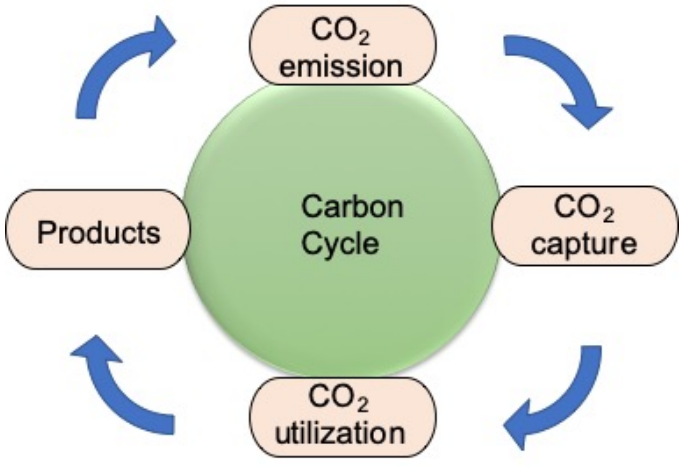

Figure 1.4. Schematic diagram of a closing carbon cycle process.

1.4 Figures of Merits

1.4.1 Open Circuit Voltage (OCV)

The OCV of SOEC is the electrochemical measurement of electromotive force limitation under the condition of the open circuit without any load. The OCV usually decreases as the temperature increases. The measured OCV is still lower than the ideal reversible voltage due to the gas phase crossover, and slight internal short circuit resulting from the tiny electricity conductivity that electrolyte has. During the electrochemical measurement, the OCV is a significant indicator of that the SOEC is operated under normal condition, which means the SOEC is not broken and has no severe leakage when OCV is closed to the ideal value. Also, through OCV measurement, the ionic conductivity of the electrolyte at the operation temperature can be obtained to evaluate the performance of electrolyte [24].

1.4.2 Current Density

Current density is the electric current flowing per unit area of the material cross-section, and it is normally used in the test of SOEC to normalize the current by area, making the measured value comparable. The current density measured versus the applied voltage is an overall quantitative assessment of SOEC performance. The current obtained can directly reflect the electrochemical reaction rate as the current is the electrons consumed or produced through the reaction per second, which represents the CO_2 reduction rate through SOEC; thus, the measurement of current density during the test is critical [25].

1.4.3 Polarization Resistance

Besides of the internal ohmic resistance brought from the electrolyte, the polarization resistance also influences the overall performance of SOEC and is a key factor in deciding the performance of electrodes. In SOEC, the polarization resistance includes the impedance behaviour at the reaction interface between electrodes and electrolyte, the kinetic resistance of electrochemical reaction, and gas diffusion during the reaction. Overall, the polarization resistance reflects the charge carriers transfer and gas phase mass transfer in the electrodes, which can be used to indicate the extent of the connection between electrodes and electrolyte, the catalytic activity of electrode catalyst, and diffusion of reactant and product [25, 26].

1.4.4 Faraday Efficiency

Faraday efficiency is used to describe the efficiency of that electrons based on the measured current is transferred to the electrochemical reaction of CO_2 reduction. Faraday efficiency is calculated by dividing the electrons CO_2 obtained in the reaction by the ideal number of transferred electrons. In SOEC, the Faraday efficiency is always evaluated to decide and analyze amount of by-products formed during the reaction, such as carbonyl [27].

1.4.5 Stability

In the SOEC, both short-term and long-term stability will be evaluated. During the stability test, the current will be measured under potentiostatic condition, or the potential can be measured at current static condition. For the potentiostatic mode, the current densities are usually measured for 15 minutes at various applied voltages to study the short-term stability. From the test, the steady state current can be observed after a period of drop from the initial current density that is very high

during cell activation. The long-term stability test runs up to hundreds of hours for lab scale experiment to obtain the cell degradation rate. The degradation rate of SOEC can indicate the decay rate of catalyst, as well as the degree of the structural integration between different SOEC components [28].

1.5 Materials of SOEC components

To fabricate the complicated SOEC, the requirements for the materials of different components are strict. Generally, the materials selected should have high conductivities, good mechanical, thermal, and chemical stability, perfect bonding between different parts, and compatible thermal expansion factors [29-31].

1.5.1 Electrolyte Material

In SOEC, the electrolyte is used to isolate two electrodes and transfer oxide ions from cathode to anode. Thus, the electrolyte should be dense enough to prevent gas phase crossover. Also, it should be very thin with satisfying ionic conductivity to provide the lowest possible internal ohmic resistance of the SOEC. Moreover, the electronic conductivity has to be small enough to prevent electron transfer and short circuit of the SOEC. Last but not least, the electrolyte needs to be redox stable under extreme oxidizing and reducing conditions [32]. Nowadays, the most commonly used electrolyte material is YSZ. Also, there are many recently researched materials such as scandia stabilized zirconia (SCSZ), samarium doped ceria (SDC), and perovskite lanthanum strontium gallium magnesium oxide (LSGM) [33-35].

1.5.2. Electrode Material

The electrodes are where CO_2 reduction and O_2 evolution occur. The materials used should have excellent catalytic activities towards them. The materials are supposed to own good ionic conductivity and electronic conductivity to provide paths for oxygen ions and electrons. Also, electrode materials should only be partially sintered at the operation temperature of SOEC. This would guarantee proper porosity and pore size that are required for the gaseous reactants and products transportation, and enough TPB area. Lastly, the materials selected need to have a similar thermal expansion coefficient with the electrolyte materials used, to prevent cell breaking caused by incompatible thermal expansion [32].

1.5.2.1 Cathode

CO_2 reduction reaction takes place in the cathode chamber of a SOEC. The development of cathode materials with high catalytic activity for CO_2 electrochemical reduction and satisfying durability is of great importance. A brief description of cathode material studied is shown below, divided into two categories: metal-cermet material and perovskite oxide material.

1.5.2.1.1 Metal-Cermet Material

Conventional metal-cermet cathodes are highly catalytically active and electronically conductive, which is directly derived from SOFC materials [36]. Nickel and YSZ (Ni/YSZ) composite material is commonly used as the SOEC cathode due to the excellent electrocatalytic activity, satisfying chemical stability, and low cost [37]. The composite electrode is widely applied in SOEC technology. It normally includes EC and IC, such as Ni and YSZ respectively, or mixed ionic and electronic conductor (MIEC) materials to provide electronic conductivity and ionic

conductivity to ensure the great transportation of electrons and oxide ions from the interface to active sites [38].

However, Ni/YSZ cathode material suffers from metal agglomeration and coking issue during the operation of SOEC [7, 31]. Operation of Ni/YSZ cathode is only feasible in reduction atmospheres such as CO_2 and CO mixture gas. In realistic condition, the redox cycle and change of the concentration of CO_2 and CO lead to the oxidation of Ni and the formation of nickel carbonyl, and the volume change associated with phase change of Ni; also, the high operation temperature results in the increased mobility and coarsening of Ni particles. The agglomeration, coking, and volume change issue all have negative impacts on SOEC long term operation and can lead to the performance degradation of the electrode [31, 39]. Ebbesen et al. have reported that the performance and degradation of their SOEC using Ni/YSZ cathode [14]. In their study, they used the 10-15 μm Ni/YSZ cathode layer and YSZ electrolyte with the same thickness. The electrochemical measurement was conducted with an operation temperature of 850 °C and mixture of CO_2 and CO atmosphere (7:3). The current density can reach 1.2 A cm^{-2} at 1.3 V, which is excellent. However, regarding the stability test using current static mode at 0.25 A cm^{-2}, the voltage and area specific resistance (ASR) increased significantly. In the first 150 hours, the voltage has been increased from 1.012 V to 1.050 V, and the ASR has been increased from 0.37 Ω cm^2 to 0.52 Ω cm^2 with a passivation rate of 0.2523 V h^{-1}. From 272 to 407 hours, the passivation rate has been increased to 0.4368 V h^{-1}. It can be seen that although Ni/YSZ cathode material has perfect electrocatalytic activity, the severe degradation issue during long term operation still limits the application of the material in SOEC. Hauch et al. have pointed out that through decreasing Ni particles sizes, mixing two phases well, and making electrodes denser will slow down the degradation rate [40]. Most recently, Ni mixed with other kinds of cermet materials, such as SDC,

with higher ionic conductivity has been studied, but the application is still restricted in electrolyzing water and not extended to CO_2 reduction [41].

1.5.2.1.2 Perovskites Material

Perovskites fall into another major category of widely used cathode catalysts thanks to their mixed ionic and electronic conductivity, and good stability [42-44]. Perovskite crystals, generally with a chemical formula of ABO_3, consist of many different compounds. In perovskite structure, rare earth metal ions, such as La^{3+}, Gd^3, and Pr^{3+}, normally occupy the A site. Also, alkaline earth metal ions like Ba^{2+}, Sr^{2+}, and Ca^{2+} can be doped into the structure to substitute the host ions to increase conductivity. Small sized transition metal ions with high catalytic activity usually occupy B site [45]. Moreover, multiple dopants can be added into both A and B site to improve the property of perovskite material, such as the amounts of oxygen vacancy and stability, leading to a range of possibilities on the application of perovskite. The following review will focus on the lanthanum strontium chromate-based perovskite material LSCrX, where X represents the transition metal dopant.

Perovskite oxide lanthanum strontium chromate manganese (LSCM) has been proved to be a suitable anode material for SOFC, and it is also used in SOEC. LSCM has excellent stability in the redox cycle and satisfying polarization resistance. However, the low catalytic activity and electronic conductivity, resulting in insufficient electrochemical performance of LSCM, still restrict the development of this material. Yue et al. have studied the performance and stability for LSCM catalyst composited with YSZ and GDC, compared with Ni/YSZ cathode, at 900 °C in different atmospheres [31]. In their experiment, the research group had fabricated the 20 mm thick YSZ electrolyte, and screen-printed Ni/YSZ (65:35), LSCM/YSZ (50:50), and LSCM/GDC

(50:50) cathode respectively. The SOECs were tested at 900 °C in the mixture gas of CO_2 and CO with different ratios. They found that Ni/YSZ cathode has the lowest polarization resistance along with the highest current density. However, when the concentration of CO increased in the feed gas, the polarization resistance increased sharply due to the carbon deposition possibly. Regarding the LSCM/YSZ cathode, it was found that the polarization resistance is twice higher than that of Ni-YSZ, leading to the significantly low current density. The difference of the polarization resistance indicates that LSCM catalyst has insufficient catalytic activity on CO_2 reduction. When LSCM is composited with GDC, the polarization resistance is improved at various applied voltages due to the higher activity from the better electronic conductivity and reduction of GDC. Also, it was found that the stability of LSCM/GDC cathode is excellent through the 200 hours stability test. At current static mode of 0.25 A cm^2, the voltage increase was only observed in the first 50 hours due to the coarsening of current collector layer, and after that period, the voltages plateaued and remained the same throughout. It can be concluded from their experiment that LSCM is a potential candidate for the SOEC operation with requirements on improving the catalytic activity [31].

$La_{0.65}Sr_{0.3}Ce_{0.05}Cr_{0.5}Fe_{0.5}O_{3-\delta}$ (LSCeCrF) perovskite catalyst has been studied in our group previously, showing the good electrochemical performance and stability [46, 47]. The LSCeCrF cathode material is derived from the traditional perovskite catalyst LSCrF with cerium doping. It has been reported that with the dopant of cerium less than 10%, the cerium can be all dissolved into perovskite structure with significantly increased amount of oxygen vacancies. The polarization resistance can decrease by about 1 Ω cm^2 when the perovskite is doped with 5% cerium compared with LSCF under SOFC operation [48]. In Yaqian et al.'s experiment, the group applied LSCeCrF as cathode material in SOEC and compared it with LSCrF. The 300 μm thickness YSZ substrate was used as the electrolyte, and the LSCeCrF and LSCrF were mixed with YSZ

(50:50) and screen printed on the electrolyte respectively. The SOECs were tested at 850 ºC in the mixture gas with different CO_2 and CO ratios. Firstly, it was found that under OCV, the SOEC has the lowest polarization resistance in the atmosphere of low CO concentration; and with the concentration of CO increased, the polarization resistance would increase gradually. The possible reason is that reducing environment makes the valance state decreasing, leading to improved electronic conductivity and increased oxygen vacancies. Regarding of the current densities, the SOEC with LSCrF cathode can reach 1 A cm^{-2} at 2 V, representing a satisfying reaction rate, but the SOEC with LSCeCrF cathode can have 1.25 A cm^{-2} at 2 V with 25% increasing. The improved electrochemical performance indicates that the dopant of cerium can effectively increase the catalytic activity of perovskite material. Besides, the short-term stability, CO production rate, as well as Faraday efficiency, were all improved through doping of cerium. It was also proved that the stability of LSCeCrF cathode was accepted while the current density only dropped by small amount under potentiostatic mode in the long-term stability test [46]. Overall, LSCrX perovskite oxide is a promising material on CO_2 reduction in SOEC, and the selection of dopant to improve the activity is required to be further studied.

1.5.2.2 Anode Material

The anode materials are important in their functions to provide active sites for oxygen evolution reaction (OER) and paths for electrons, oxygen ions, reactants, and products. It is required that the material used for anode has an excellent activity to ensure that the ions transferred to the anode can be oxidized to O_2 and released right away. Lanthanum strontium manganese (LSM) and lanthanum strontium cobalt ferrite (LSCF) are state of the art anode materials for SOEC, and the following review will focus on these two materials. [49].

LSM is a most common anode material for SOEC due to its excellent electrocatalytic activity for OER, satisfying electronic conductivity, and good chemical compatibility with electrolyte. However, the performance of LSM is limited by the low ionic conductivity especially when the temperature is reduced, causing the decreased length of TPB as the reaction only takes place in a small area at the interface of anode and electrolyte. Also, when LSM is composited with YSZ by traditional mixing method, the unstable structure will be formed due to the non-uniform distribution of two particle grains, leading to performance degradation. Liang et al. have proposed a different way to generate a uniform distribution of particle grains [50]. In their experiment, during the synthesis of catalyst powders using nitrate combustion method, the YSZ powders were directly added into the precursor solution. Unlike the morphology of anode fabricated using the powders made by mixing as prepared LSM powders with YSZ through ball milling directly where LSM grains are obviously smaller than that of YSZ, the grain sizes are equivalent for two powders which significantly extend the length of TPB. Regarding the electrochemical performance, it has a 50% improvement on current density using the new method. The excellent chemical compatibility between LSM and YSZ is an attractive aspect for LSM, because LSM can keep integrated perovskite structure when contact with YSZ at high temperature. Thus, for the wider application of LSM in SOEC, the improvement of ionic conductivity and optimization of composite cathode structure have to be further studied [50].

LSCF catalyst is widely used as SOEC anode. It has excellent ionic and electronic conductivity even at a lower temperature. Also, the oxygen vacancy concentration and surface exchange rate of LSCF are very high, making LSCF an eligible candidate for SOEC application. However, the electrocatalytic activity is insufficient, and long-term stability is critical due to the reaction between LSCF and YSZ. It is found that the interface between LSCF and YSZ is very

reactive. The La and Sr ions in the perovskite structure can react with zirconia in YSZ to form an electrically insulating layer at the interface, significantly leading to the decrease electrochemical performance [51]. To solve the interaction problem, a GDC interlayer between LSCF and YSZ is commonly used [52]. Kim et al. have studied the influence of GDC interlayer on resistance and stability [53]. In their experiment, they fabricated a SOEC with YSZ electrolyte and a 4 μm thick GDC interlayer, and the SOEC is sintered at various temperatures to observe the effect of temperature on the formation of GDC interlayer. The SOEC without GDC interlayer was also fabricated to compare. Firstly, it was found that at sintering temperature of 1300 °C, the SOEC had the most stable performance after 100 h long term stability test with the lowest resistance. Moreover, they found that with GDC interlayer, the polarization resistance only slightly increased after 50 hours (less than 0.1 Ω cm^2) and the ohmic resistance remained the same. However, the polarization resistance of the cell without interlayer increased sharply, which is about twice as the initial value; not only the increase of polarization resistance was observed, the intrinsic ohmic resistance demonstrated a significant increase as well [53]. Under the circumstance that GDC interlayer can effectively improve the stability, unfortunately it also leads to the increase of ohmic resistance due to the insulating layer formed between GDC and YSZ resulted from the interaction at such high temperature [54]. Overall, LSCF is a suitable anode catalyst material for OER in SOEC which has satisfying reaction rate, but the long-term stability has to be improved.

1.5.3 Buffer Layer

The GDC interlayer mentioned before is also called buffer layer. The buffer layer is an optional component in SOEC, which is needed when the electrode materials are not chemically compatible with electrolyte. Generally, GDC is used as buffer layer in SOEC due to GDC has high

ionic conductivity as well as good compatibility with both electrode and electrolyte materials. However, the elemental migration still exists by surface phase and gas phase diffusion through the pores in the buffer layer, even if physically separate electrode and electrolyte layer can prevent the interaction somehow. Completely sintering of the GDC buffer layer without any pores is still a severe issue [55]. The sintering temperature should be controlled under 1250 °C as the temperature above this will lead to the reaction between GDC and YSZ electrolyte layer to form the insulating material. But the GDC can only be fully sintered at the temperature above 1400 °C. The commonly used sintering aid to decrease sintering temperature is also difficult to be applied here because adding of sintering aid will lead to the increased possibility of complicated side reactions sometimes and the rapid shape change brought by the sintering aid, resulting in the structural instability [56].

To generate the GDC buffer layer without percolated pore and prevent the reaction between GDC and YSZ at the meanwhile, Lee et al. have proposed a design of diffusion block buffer layer. In their experiment, the buffer layer was fabricated in two layers. For the bottom layer, they used the particle-dispersed glycine nitrate process (PD-GNP) to fabricate bimodal nanoparticles. The glycine nitrate precursor solution with stoichiometric amounts of gadolinium (Gd) and cerium (Ce) was mixed with inclusion particle slurry including the commercial larger sized GDC powders to generate equally distributed GDC powders with two sizes. Regarding the top layer, GDC powders were generated with cobalt as sintering aid. By modifying the thickness of two layers, contents of cobalt, and sintering process and temperature, the dense buffer layer can be generated. In the SOFC mode, they found that ohmic resistance, as well as the polarization resistance, decreased due to the elimination of pores, and facilitation of surface exchange process and ion transport between electrode and electrolyte through the diffusion block layer, thus the current density was also

increased. Besides the improvement on electrochemical performance, the effect of diffusion block buffer layer on stability was also obvious. For the long-term stability around 1000 hours, the cell with the diffusion block buffer layer only experienced 5 mV degradation while the cell with traditional buffer layer had over 60 mV voltage degradation. It can be concluded that the diffusion block buffer can improve not only the performance of the SOFC but also increase the stability. This technology may be able to apply to SOEC as well [51].

1.6 Electrode Fabrication Methods

Besides the intrinsic catalytic activity, the morphology of electrodes, particularly the active specific surface area, is also essential to the performance of SOEC [57]. Thus, the following review will introduce two state of the art technologies, infiltration and in-situ exsolution, which can be used to optimize the microstructure of electrodes.

1.6.1 Infiltration

Infiltration is an effective way to add a variety of catalysts into the electrodes, therefore enhancing the cell performance and reliability. Active electrodes fabricated using infiltration consist of a porous backbone with ionic and electronic conductivity and active coating catalysts with high catalytic activity and stability [58]. The schematic diagram illustrating typical steps of the infiltration process is shown in Figure 1.5. The first step is the preparation of porous backbone, which is shown in Figure 1.5 (a). During the procedure of sintering at very high temperature, the backbone can form excellent bonds with electrolyte, ensuring the structural stability of electrodes under the operating condition and the satisfying connectivity for conduction of oxygen ions and electrons. The second step is infiltration of the catalyst solution, which is the electro-active surface phase, shown in Figure 1.5 (b). The infiltrated solution or sol is prepared by mixing precursors

containing stoichiometric metal salt with desirable complex agents or surfactants, and then the solution or sol is introduced into the pre-fired backbone. After proper heat treatment, two typical morphologies, discrete particles (Figure 1.5(c)) or continuous thin film (Figure 1.5(d)), can form. The thermal treatment required to form the desired phases of catalyst coated on the electrodes using infiltration technique uses much lower heating temperature than the heat treatment needed for forming the backbone. A new catalyst layer with multi-functionality utilizing the properties of catalyst and backbone can be produced. It is required that the catalysts are not supposed to react with the electrode backbone to prevent loss of electrocatalytic activity and presence of undesired phase during the high temperature operation, resulting in the long-term stability attenuation. The different morphologies, which can be controlled by infiltrated solution, is proved to have a great influence on electrodes performance [58]. The viscosity of the infiltrated solution is a key factor of the morphology of the catalyst layer. Dillen et al. mentioned that infiltration solution with low viscosity can help to yield the uniform catalyst layer as well as the secure bonding between catalyst layer and electrolyte, while high viscosity may cause the non-uniform distribution of catalyst [59]. The viscosity mainly depends on the type and amount of surfactant used and the concentration of metal ions. A large number of surfactants such as ethylene glycol and polyvinyl alcohol should not be applied in the configuration of infiltrated solution to prevent homogenous and viscous gel may formation during heating. Regarding the concentration of metal ions, although concentrated solution may be preferred on reducing infiltration cycles, it will also cause the difficulties of solution penetration into the entire backbone and uniform distribution of catalyst [60].

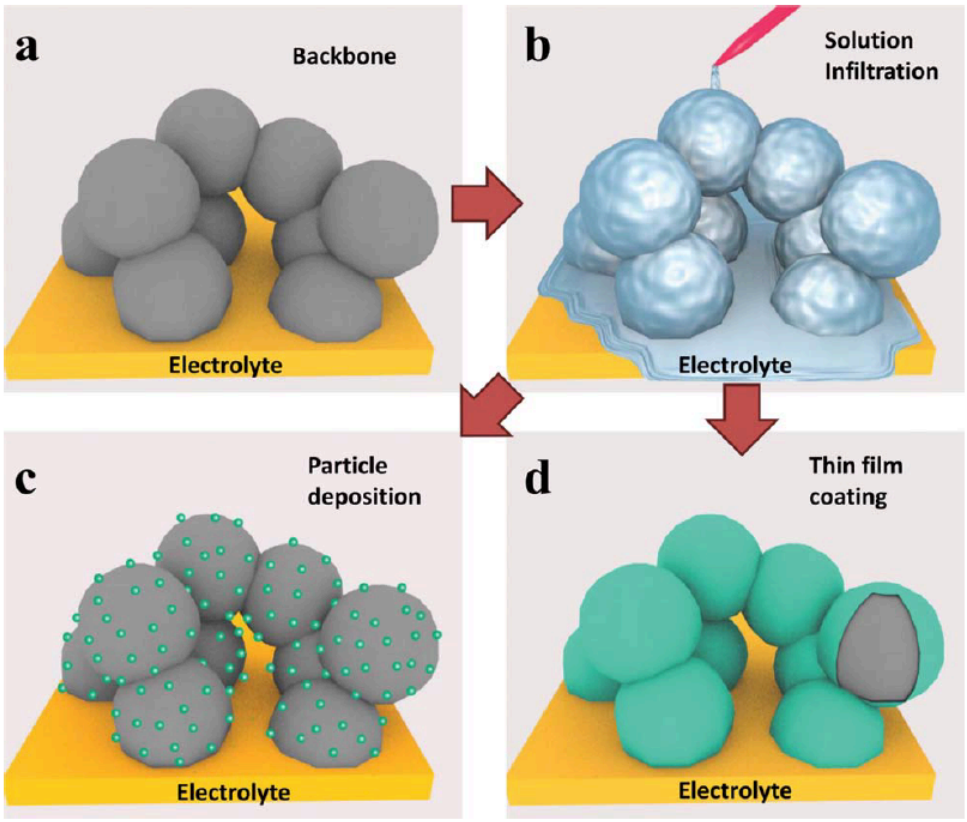

Figure 1.5. Schematic diagram of a typical infiltration process: (a) an as-prepared electrode backbone; (b) catalyst solution infiltration into backbone; (c) and (d) two typical morphologies of infiltrated electrode, particle deposition and thin film, after treatment [58]. Ref. 58 from Royal Society of Chemistry, Copyright 2019.

1.6.2 In-situ Exsolution

In the in-situ exsolution, the active metallic elements are firstly doped into B-site of a perovskite during synthesis, and then active nanoparticles (NPs) can in-situ exsolve from the perovskite oxide lattices under a reducing environment, as shown in Figure 1.6. The metallic nanosized catalysts produced by in-situ exsolution have enlarged the specific surface area that results in the enhanced electronic conductivity and active TPBs. Also, as the active metallic elements are in-situ exsolved from the perovskite lattice, the active NPs are evenly distributed on

the surface of perovskite oxides. More importantly, due to the strong bonding between the NPs and the lattices, the catalyst degradation caused by grain coarsening issue of NPs under high-temperature operation conditions can be significantly alleviated [61-63].

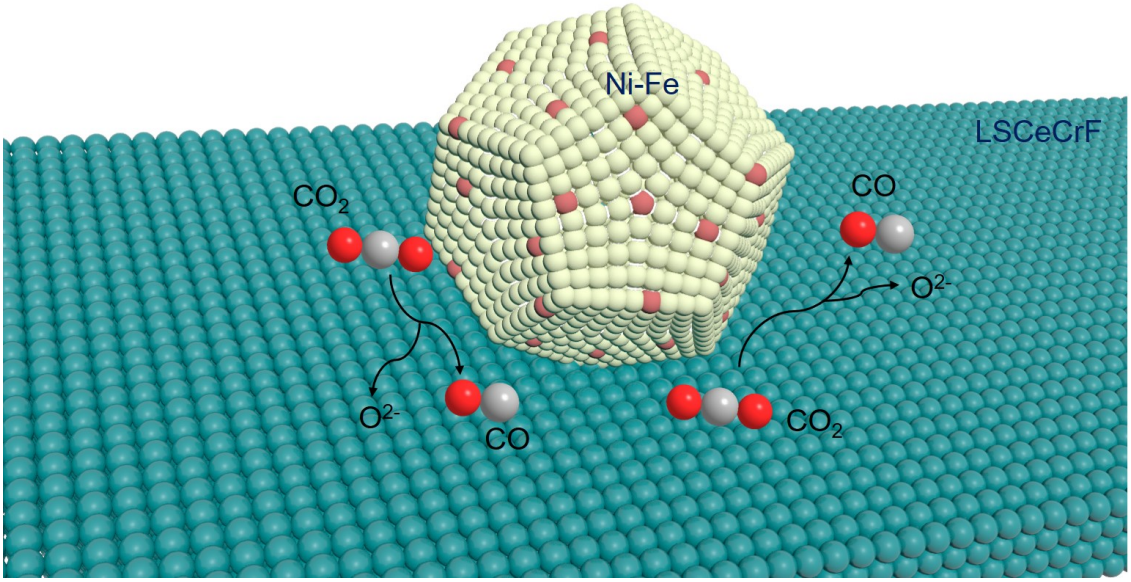

Figure 1.6. Schematic Diagram of in-situ exsolution of Ni-Fe NPs from perovskite structure.

It was recently found that the A-site deficient perovskite oxide structure, which means A/B<1, is more preferred to exsolve the doped cations even for the active metals which are hard to be reduced on the surface of the structure. To produce a perovskite structure with various NP compositions which have even distribution and satisfying coverage, A-site deficiency is an effective way to facilitate B-site in-situ exsolution. Perovskite structure naturally tends to be stable as ABO_3 and without any defects. Therefore, the B-site cation is energy favorable to be exsolved from the structure to make it stable [64]. Ye et al. have studied the effects of in-situ exsolution of Ni from A-site deficient chromite and magnesium doped lanthanum strontium titanium (LSTC and LSTM). It was found that with in situ exsolution of nickel particles, LSTC can reach a current

density of 0.75 A cm^{-2} and LSTM can reach 0.87 A cm^{-2} at 2 V under 800 °C, where both of them had 20% improvement on current densities compared with these without in situ exsolution. The polarization resistances for the catalyst with Ni exsolved are also decreased significantly. The reason for the improved electrochemical performance is that both chemical adsorption and desorption are increased when the metallic nanoparticles proved by the infrared spectroscopy and temperature programmed desorption (TPD) test, as well as the theoretical calculations. As for in situ exsolution, the reduction of metal oxide and exsolution of metallic NPs will generate neighboring oxygen vacancies, and the oxygen vacancies close to the active catalytic sites can provide a reactive site for CO_2 adsorption and lower down the desorption temperature. Furthermore, the long-term stability for the exsolving cathode material is satisfying while there is no degradation (current drop) observed at the applied voltage of 1.3 V over 100 hours. The enhanced stability at high operation temperature and good coking resistance of exsolved NPs are resulted from the strong interface between metallic NPs and perovskite oxide structure by the anchoring effect [39]. Therefore, in-situ exsolution is treated as a promising way on incorporation of active NPs on perovskite structure to improve both activity and stability of catalyst in SOEC.

1.7 Challenges

Previous studies from our group have shown that $La_{0.65}Sr_{0.3}Ce_{0.05}Cr_{0.5}Fe_{0.5}O_{3-\delta}$ (LSCeCrF) perovskite catalyst as SOEC cathode has great electrochemical catalytic activity for CO_2 reduction with stable CO output under various bias voltages [46, 47]. However, the catalytic activity of this catalyst is still limited by the active specific area. Infiltration is an efficient way to increase the triple phase boundary (TPB) by building a nanostructured electrode for the improvement the electrolytic efficiency [66]. Also, the electronic conductivity and activity of such perovskite

material are inferior to that of metallic materials [65]. Thus, the incorporation of metallic catalysts into perovskite cathode is wanted to utilize their complementary advantages [67]. However, the infiltration of highly active metallic NPs, such as Ni that has excellent catalytic activity towards CO_2 reduction, still faces the agglomeration problem during the high-temperature sintering and operation [68]. The infiltrated in-situ exsolution method has been proposed to disperse evenly distributed and thermally stable metallic NPs compared to the conventional infiltration method to further optimize cathode microstructure on the improvement of catalytic activity, electronic conductivity and stability.

1.8 Objective and Thesis Contents

As discussed in section 1.5.2.1.2, and 1.7, the perovskite oxide LSCeCrF is a potential candidate for the cathode material of SOEC with satisfying performance and stability, but also faces challenge of insufficient specific surface area. The objective of this thesis is to optimize the microstructure of the cathode LSCeCrF to improve the electrochemical performance through enhancement of catalytic activity by increasing active specific area, and the stability of SOEC using infiltration and in-situ exsolution.

Chapter 2 introduces the methodology, including material synthesis, cell fabrication, electrochemical test setup for SOEC, electrochemical measurements, as well as characterization methods.

Chapter 3 will focus on optimization of LSCeCrF cathode microstructure through infiltration. The morphology of cathode, electrochemical performance including current density, resistance, CO production rate, and Faraday efficiency, as well as the stability, will be

characterized and measured. The results are compared with that of the previous study on LSCeCrF using conventional electrode fabrication method.

In Chapter 4, the microstructure of SOEC cathode is optimized through the in-situ exsolution of Ni-Fe NPs from the A-site deficient $(La_{0.65}Sr_{0.3}Ce_{0.05})_{0.9}(Cr_{0.5}Fe_{0.5})_{0.85}Ni_{0.15}O_{3-\delta}$ (Ni-LSCeCrF). The obtained nanostructured electrode was confirmed by the microstructural characterizations. Also, X-ray diffraction and transmission electron microscope were used to characterize the content of exsolved NPs. The density function theory (DFT) [69, 70] was also adopted to theoretically investigate the in-situ exsolution behavior of Ni and Fe elements from LSCeCrF perovskite matrix. The electrochemical performance and redox stability of Ni-LSCeCrF cathode material in a SOEC for CO_2 electrolysis have been measured and compared with the previous study based on LSCeCrF cathode material [46].

Conclusions and future work will be summarized in Chapter 5.

Chapter 2 Methodology

2.1 Materials synthesis

The cathode material, LSCeCrF and Ni-LSCeCrF, was synthesized *via* the glycine-nitrate combustion method. The glycine-nitrate combustion method to synthesize oxide ceramic powders was first created by Pacific Northwest Laboratory in 1990. As shown in Figure 2.1, stoichiometric ratios of metal nitrates combining with glycine were dissolved in aqueous solution to prepare the precursor. The precursor solution was then stirred and heated to evaporate water and form the viscous solution. After the solution becomes viscous enough, the heating temperature raised to about 180 °C can lead to the self-ignition. The flame brought by rapid and drastic combustion with temperature between 1100 °C and 1400 °C can help to form the perovskite oxide with homogenous compositions. Finally, the as-prepared powders are calcined at a specific temperature, depends on the material, to decrease residual carbons and eventually produce the uniform perovskite structure. The powders synthesized by nitrate combustion method have the advantages of smaller particle sizes, excellent composition uniformity, and low residual carbons [71].

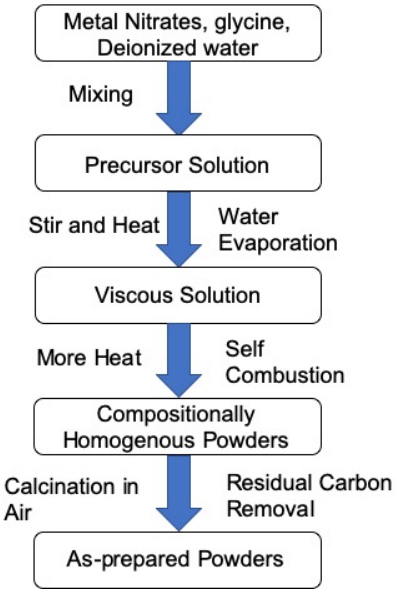

Figure 2.1. Material Fabrication Flow Chart by Nitrate Combustion Method

2.1.1 Synthesis of LSCeCrF

Stoichiometric amounts of La $(NO_3)\cdot 6H_2O$, Sr $(NO_3)_2$, Ce $(NO_3)_3\cdot 6H_2O$, Cr $(NO_3)_3\cdot 9H_2O$, and Fe $(NO_3)_3\cdot 9H_2O$ were first dissolved into deionized water. Glycine was added into the solution with the molar ratio of 2:1 to the total amount of the metal cations. The solution was heated under vigorous stirring on a hot plate to induce self-combustion. The LSCeCrF were obtained by calcination in air for 4 hours, followed by reducing in hydrogen for 6 hours at 900 °C. The hydrogen treatment was applied to enhance the crystallization of the as-prepared LSCeCrF powders.

2.1.2 Synthesis of Ni-LSCeCrF

Stoichiometric amounts of La $(NO_3)\cdot 6H_2O$, Sr $(NO_3)_2$, Ce $(NO_3)_3\cdot 6H_2O$, Cr $(NO_3)_3\cdot 9H_2O$, Fe $(NO_3)_3\cdot 9H_2O$, and Ni $(NO_3)_2\cdot 6H_2O$ were first dissolved into deionized water. Glycine was

added into the solution with the molar ratio of 2:1 to the total amount of the metal cations. The solution was heated under vigorous stirring on a hot plate to induce self-combustion. The Ni-LSCeCrF were obtained by calcination in air for 4 hours, followed by reducing in hydrogen for 6 hours at 900 °C. The hydrogen treatment was applied to enhance the crystallization of the as-prepared Ni-LSCeCrF powders and simultaneously trigger out the exsolution of metallic nanoparticles. For better observation of in situ exsolution, we also fabricated a Ni-LSCeCrF pellet by die-pressing and sintering in air at 1200 °C for 10 h, and being reduced in hydrogen at 900 °C.

2.2 Cell fabrication

The SOEC cell was fabricated using the commercial YSZ substrate with the thickness of 300 μm and diameter of 25 mm as the electrolyte. $Gd_{0.1}Ce_{0.9}O_{1.95}$ (GDC) buffer layers were fabricated between electrodes and YSZ electrolyte by screen printing to prevent chemical incompatibilities. Commercial GDC powder was mixed with 4% ethyl cellulose at a ratio of 6:4 to form the slurry. The slurry was then screen printed on both sides of the electrolyte and sintered at 1300 °C for 10 h. After that, the GDC slurry was brush-printed on both sides of the cell and sintered at 1250 °C to form the cathode/anode scaffolds. The electrode scaffold shows a geometric area of 0.5 cm^2 and a thickness of ~ 40 μm. Both cathodes, LSCeCrF and Ni-LSCeCrF, and anode catalysts, $La_{0.6}Sr_{0.4}Co_{0.2}Fe_{0.8}O_{3-\delta}$ (LSCF), were deposited on the surface of GDC scaffolds with 20 wt.%-30 wt.% loading via infiltration method. After the infiltration, the cell was sintered in air at 900 °C for 4h to form catalyst particles in the scaffolds.

2.3 Electrochemical Test Setup for SOEC

The gold paste was printed on the surfaces of both electrodes to form current collectors. The silver wire with a diameter of 0.5 mm was then connected to the current collectors using gold paste. The cell was sealed on a coaxial two-tube setup, where the outer edge of the anode side was stuck to the outer tube using Ceramabond 552 to avoid the leakage of gas. The cell was tested in an MTI tubular furnace. The schematic diagram for the structure of fabricated SOEC and electrochemical test setup is shown in Figure 2.2. Hydrogen was first fed to reduce the catalyst at 900 °C. After reduction, carbon dioxide and carbon dioxide mixed with carbon monoxide were fed at a rate of 100 mL min^{-1} as the inlet gases. The outlet gases from the anode side were evaluated by gas chromatography (GC). The anode chamber is exposed to air for exsolution of O_2 gas.

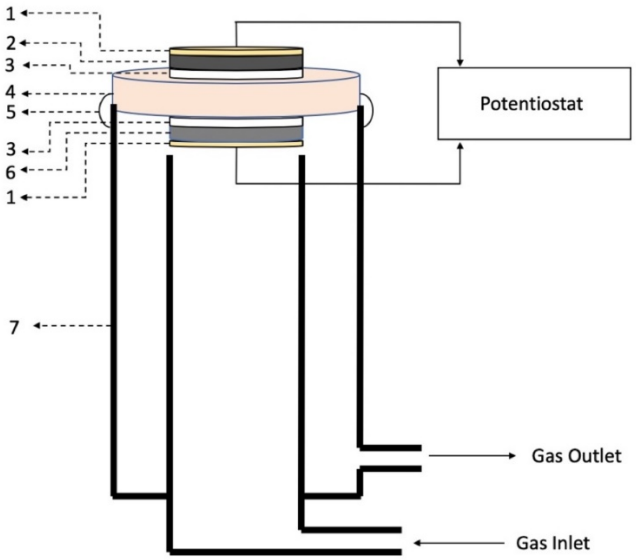

Legend:
1. Gold Current Collector
2. Anode: LSCF/GDC
3. Buffer Layer: GDC
4. Electrolyte: YSZ
5. Ceramabond 552
6. Cathode: LSCeCrF/GDC and Ni-LSCeCrF/GDC
7. Coaxial Two-tube Setup

Figure 2.2. Schematic Diagram of the Fabricated SOEC Structure and Electrochemical Test Setup.

2.4 Electrochemical Measurements

The electrochemical performance was measured using an electrochemical workstation of a Solartron 1287 instrument and a Solartron 1255B frequency response analyzer.

2.4.1 Polarization Curves, Stability curves, and Faraday Efficiency

To ensure the interconnect resistance will not influence the electrochemical performance of SOEC, a four-point probe measurement was applied. The polarization curve was measured under the potential dynamic mode. The current densities were measured and recorded under various voltages from OCV to 2V with a ramping rate of 20 mV per second. Regarding of the short-term stability, the current densities were recorded at various applied voltages (1.2V, 1.4V, 1.6V, 1.8V) under potentiostatic mode for 15 minutes at each voltage, and at the meanwhile, the outlet gas was collected by the GC to obtain outlet gas compositions. The CO production rate, as well as CO faraday efficiency, can be calculated from the gas compositions and the corresponding current densities. The long-term stability was tested by measuring current density versus time at an applied voltage of 1.6 V for 100 hours.

2.4.2 Electrochemical Impedance Spectra

Electrochemical Impedance Spectra (EIS) is a powerful measurement for SOEC characterization that can determine dielectric properties (resistive and capacitive). In EIS, through the small perturbation of voltage and the current feedback, impedance spectroscopy can be obtained as the function of frequency. The internal ohmic resistance, polarization resistance, and losses from the mass transfer are able to be distinguished to characterize the electrochemical performance of SOEC. Figure 2.3 shows a typical impedance spectroscopy obtained from EIS.

The x-axis of the graph shows the real components of impedance, indicating the resistance that does not change with frequency. The y-axis stands for the imaginary components, representing how the impedance changes with frequency [25]. The interception of the curve with the x-axis is the ohmic resistance of SOEC, Rs, including the resistance from electrolyte, electrodes, and interconnects. The rest part, R_p, is the polarization resistance of the SOEC, which can be further divided by the two arcs into high-frequency $R_{H,}$ and low frequency, R_L. Unlike the EIS in SOFC that can clearly recognize activation polarization from cathode and anode, the high frequency and low-frequency resistances obtained from the two arcs for SOEC cannot be simply treated as the resistances brought by cathode and anode respectively. For the high-frequency resistance, which is mainly composed of the oxygen ion transport across the interface between anode and electrolyte, and the interaction of gas and solid phase at the catalyst functional layer of cathode. Regarding low-frequency resistance, it represents the chemical surface exchange of anode and the gas diffusion of cathode side [51].

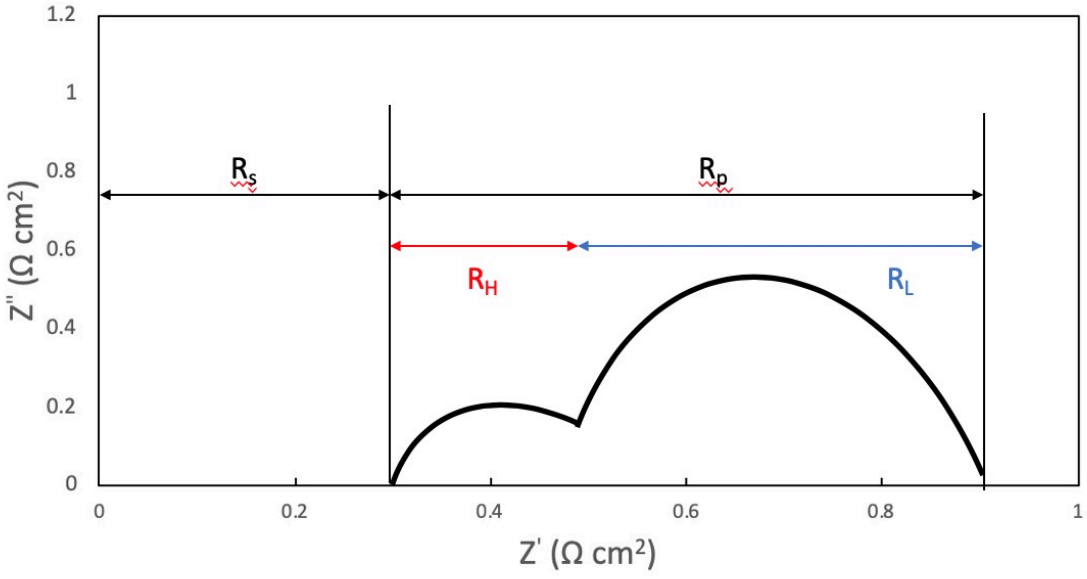

Figure 2.3. Typical Diagram of Impedance Spectroscopy for EIS.

In this experiment, the EIS was conducted at both atmospheres, pure CO_2 and mixture gas at different voltages (OCV, 1V, 1.2V, 1.4V, 1.6V, and 1.8V) from 10^5 to 0.1 Hz with 20 mV sinuous alternative current (AC) amplitude. The experimentally measured data were further analyzed by using equivalent circuit modeling through Zsimpwin software.

2.5 Characterization Methods

2.5.1 X-ray diffraction

X-ray diffraction (XRD) can determine the crystalline phase of the material powders. Besides of the components, XRD is also useful on identify grain size of NPs, lattice defects, and lattice parameters. During the XRD test, the incident X-ray is generated and directed toward samples. The X-ray beam will be diffracted by atoms in the crystalline with a specific angle of incidence, θ. The distance between the crystalline atomic layers, d, can be obtained when the wavelength λ of X-ray is known using Bragg's law: $n\lambda = 2d \sin \theta$, where n is an integer. In the experiment, the catalyst phase formation was analyzed by XRD using a Rigaka D/max-2500 X-ray diffractometer with Co Kα radiation at a scan range of 10 degree to 110 degree and a scan rate of 2 degree/minute, and the obtained data were analyzed using Xpert Highscore Plus software.

2.5.2 Scanning transmission electron microscope and energy dispersive X-ray spectroscopy

Scanning transmission electron microscope (STEM) is a popular and widespread technique recently. For the STEM, the finely focused electron beam in a raster pattern scans across the thin sample, and the signal stream will be generated from interactions between them. The virtual image can be built through the signal stream after it is correlated with the beam position. The most significant advantage of STEM is high spatial resolution. The energy dispersive X-ray

spectroscopy (EDX) is usually combined with STEM to obtain the elemental mappings for the sample. For scanning transmission electron microscope energy dispersive X-ray spectroscopy (STEM-EDX), the electron beam with high intensity is used to excite an electron from the inner shell of the sample atom to create an electron-hole pair. Then, an electron with higher energy from the outer shell will fill the hole generated. The energy difference will be released in the form of X-ray and detected. As all the element has the unique energy difference between each shell depending on the atomic number, the X-ray can be used to characterize the types of elements as well as the quantities [72]. The elemental mapping of as-synthesized Ni-LSCeCrF was analyzed by the JEOL JEM-ARM200CF STEM-EDX

2.5.3 Field emission scanning electron microscope

The field emission scanning electron microscope (FESEM) is the microscope which uses negatively charged electrons liberated by field emission source to scan the sample in the zigzag pattern. In the high vacuum environment, the primary electrons are accelerated in the high electrical field gradient and bended to the narrow scan beam to bombard the sample surface. The secondary electrons that are emitted from the sample with specific angles and velocities can reflect surface structure. Secondary electrons are then caught by the detector to be transformed to electric signal. A digital image can be produced automatically after the signal is amplified. The in situ exsolution of NPs on Ni-LSCeCrF pellet was characterized through Zeiss Sigma 300 VP FESEM. The micromorphology of the cell was also examined using the FESEM.

Chapter 3 Microstructure Optimization through Infiltration of LSCeCrF

The SOEC with cathode using perovskite oxide LSCeCrF fabricated by conventional method has been proved to have good electrochemical performance on CO_2 reduction, but the catalytic activity is still limited. Optimization of cathode microstructure is an effective way to improve the activity by increasing active specific area. In this chapter, infiltration of LSCeCrF was applied for microstructural optimization. The effect of infiltration on active specific area enhancement was confirmed through the morphology analysis and electrochemical measurement.

3.1 XRD Analysis for LSCeCrF powders

The typical calcination temperature to form the single phase of LSCeCrF perovskite is above 1100 °C [73]. However, when incorporating the infiltration method, a lower temperature is preferred to avoid the aggregation of nanosized catalyst. In this study, we reduced the calcination temperature to 900 °C for LSCeCrF. Figure 3.1 shows the XRD patterns of the as-prepared LSCeCrF powder. Compared with the standard pattern of $LaCrO_3$ (PDF: 01-075-0288), the cubic perovskite phase was formed with impurity remained after sintering in the air at 900 °C for 4 h. Small peaks representing the existence of minor phase $SrCrO_4$ can be observed in the patterns of as-prepared LSCeCrF. T. Wei *et al.* found that hydrogen treatment after the calcination in the air can promote the single phase formation of lanthanum strontium chromite ferrite (LSCrF) by enhancing the crystallization of the as-prepared powder [74]. In their experiment, LSCrF perovskite structure can be formed after reduced in hydrogen, and the electrochemical performance of the catalyst was not influenced. This phenomenon was confirmed in this work. After the

reduction in hydrogen at 900 °C for 6h, the minor impurity phase in as-prepared LSCeCrF disappeared due to the dissolution of $SrCrO_4$ under the reduction atmosphere and a single perovskite phase formed. The hydrogen treatment can effectively lower the perovskite structure formation temperature, which is significantly important for infiltration method. This step is critical for microstructure optimization of electrodes to maintain the sizes of catalyst NPs during the fabrication process.

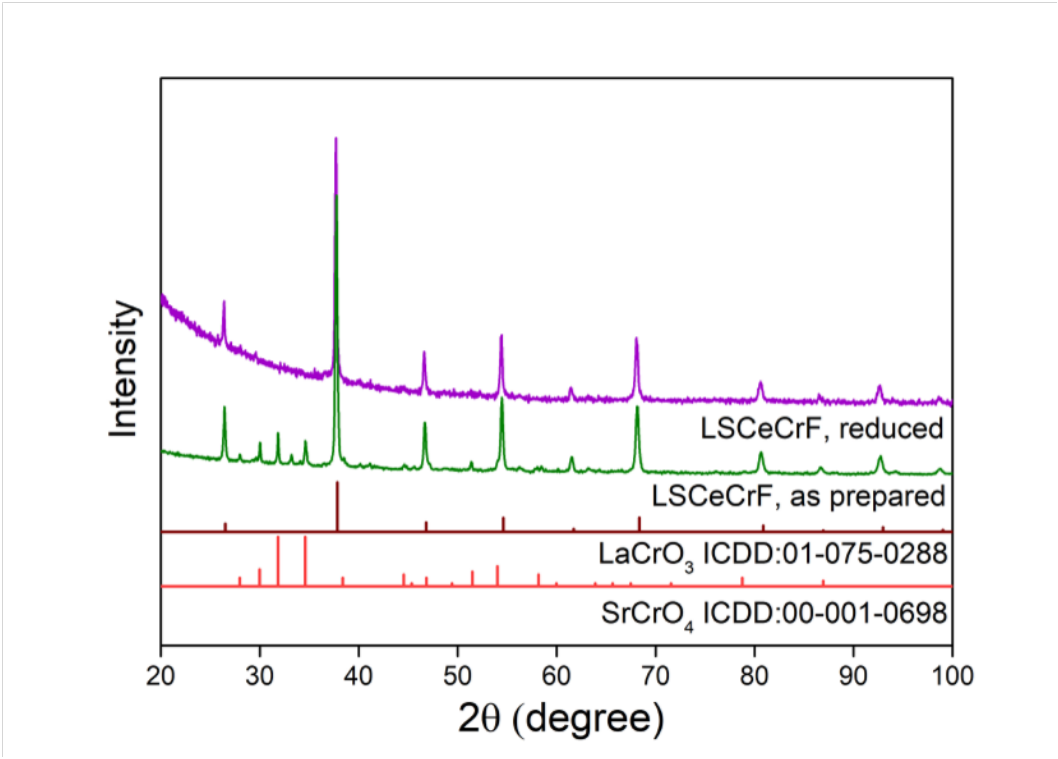

Figure 3.1. XRD patterns of the as-prepared and reduced LSCeCrF.

3.2 Morphology Analysis of SOEC with infiltrated LSCeCrF cathode

The cross-section of fabricated SOEC with a YSZ electrolyte in the middle, and a cathode on the top and an anode on the bottom is shown in Figure 3.2 (a). The commercial YSZ electrolyte has a thickness of 300 μm. The electrodes have thickness around 30-40 μm while the GDC buffer

layer is about 5 μm thick as shown in Figure 3.2 (b). The interface between cathode and electrolyte is shown in Figure 3.2 (c). The porous cathode is firmly bonded with the dense YSZ electrolyte, which will ensure the fast transfer of oxygen ions between electrodes and electrolyte.

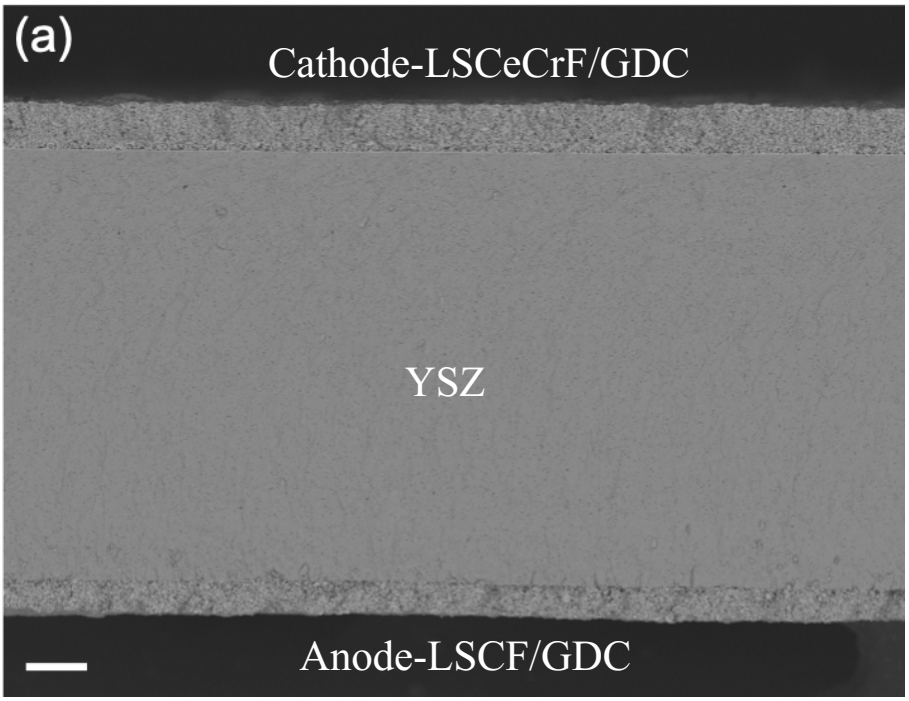

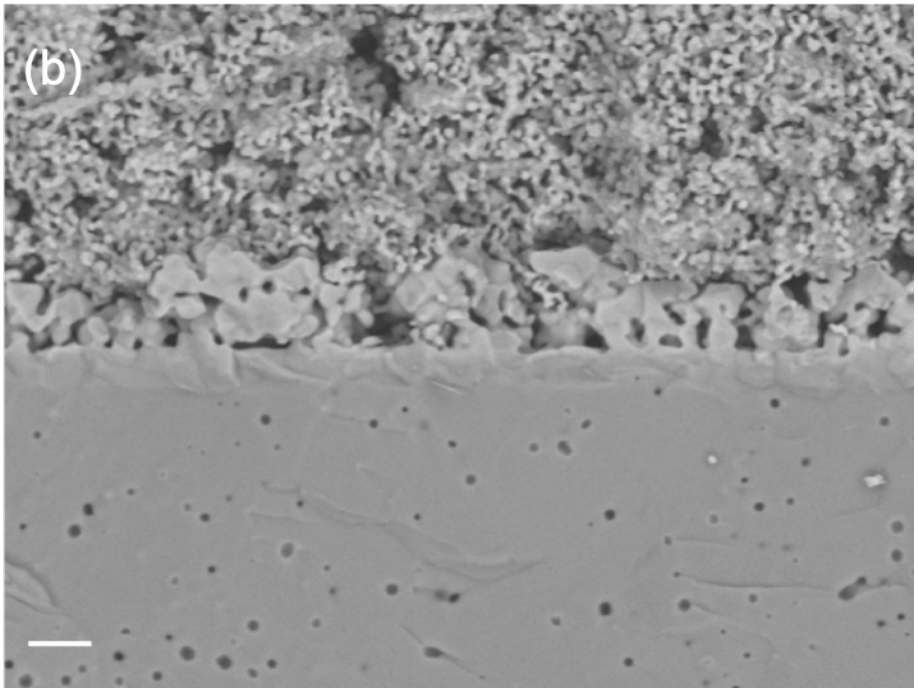

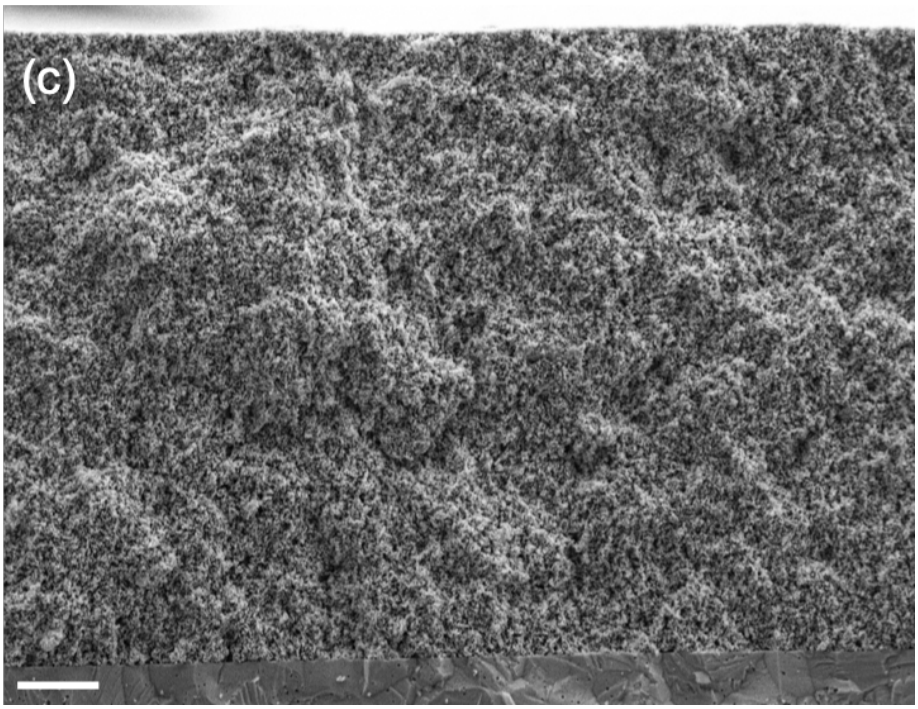

Figure 3.2. FESEM images of (a) the cross-section of fabricated SOEC with LSCeCrF+GDC/YSZ/LSCF+GDC (scale bar, 40 μm), (b) the interface between anode, buffer layer, and electrolyte (scale bar, 2 μm) , and (c) the interface between cathode and electrolyte (scale bar, 10 μm).

Figure 3.3 shows the micromorphology of the GDC scaffold without and with LSCeCrF infiltration. It can be seen that the surface of GDC particles without infiltration is very smooth (Figure 3.3 (a)), while the surface becomes rough after catalyst infiltration and reduction treatment (Figure 3.3 (b)), indicating the formation of continuous thin film consisting of catalyst nanoparticles. Unlike the conventional cathode fabrication method which mechanically mixes the perovskite oxide with YSZ or GDC, the TPB and reaction area of cathode fabricated by infiltration can be significantly extended by the well distributed LSCeCrF NPs [46]. Through infiltration, the porous cathode can provide excellent electronic and ionic conductivity. At the meantime, the active surface area of the catalyst is greatly increased, which will improve the electrocatalytic activity of cathode on CO_2 reduction.

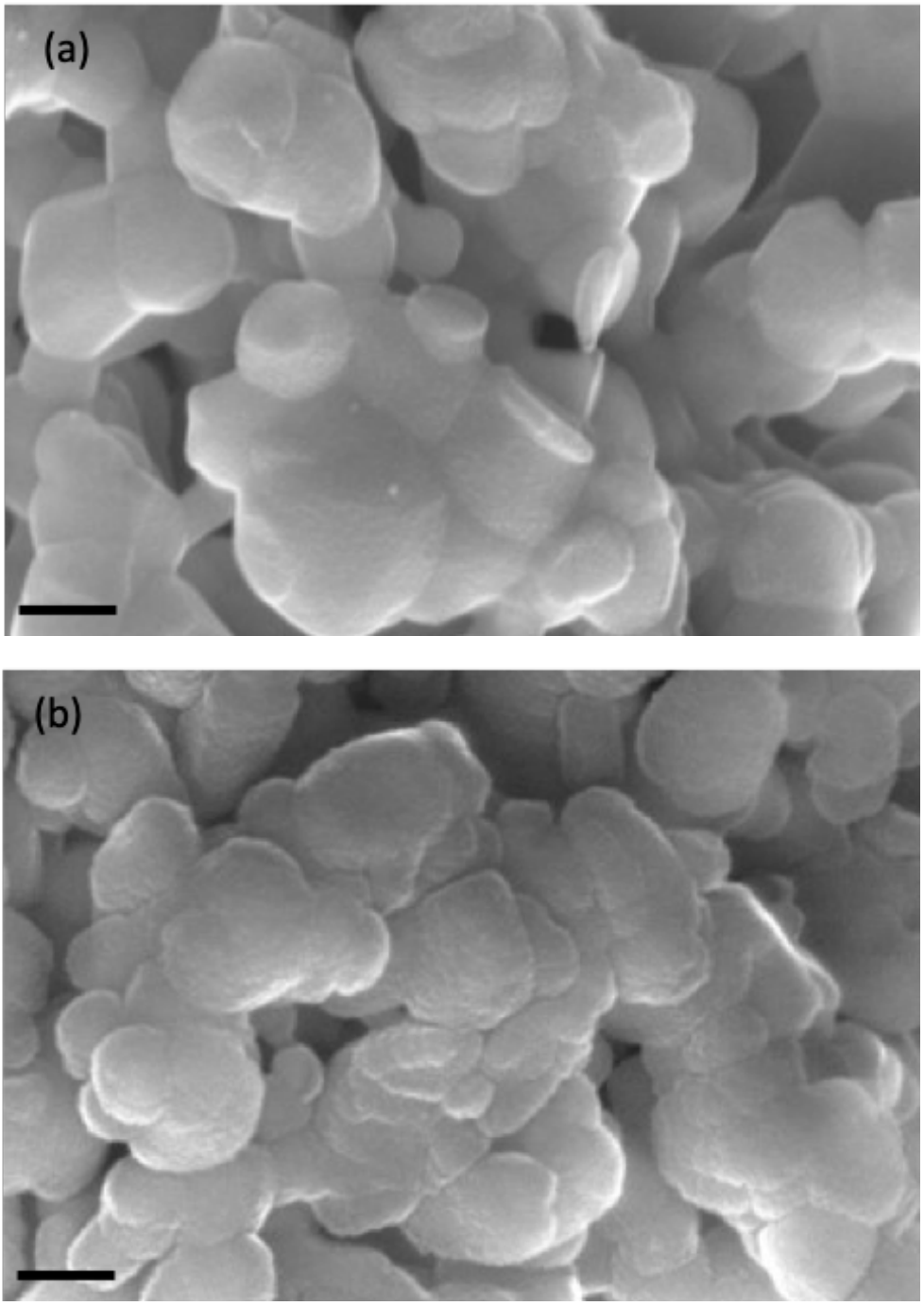

Figure 3.3. FESEM images of the cross-section of GDC scaffold (a) without and (b) with LSCeCrF infiltration (scale bar, 200 nm).

Figure 3.4 is the FESEM image of the cathode fabricated by conventional method. It can be seen that through nitrate combustion method, fine particles with a homogenous size that less than 100 nm can be produced. Also, two phases in the composite cathode are well distributed, which can increase the reaction area [46]. However, the active reaction area still composes of two phases with EC and IC separately, leading to the decrease of active specific area. Compared to the cathode fabricated by conventional method, the infiltration method can form a thin film of catalyst on the GDC backbone to fabricate a new functional catalyst layer. The unique properties for two different materials, the perovskite oxide and the backbone, can be combined to form a new structure with multifunctionality [75]. The whole porous cathode structure became to a MIEC material with combined properties, significantly enhancing the TPB and reaction area.

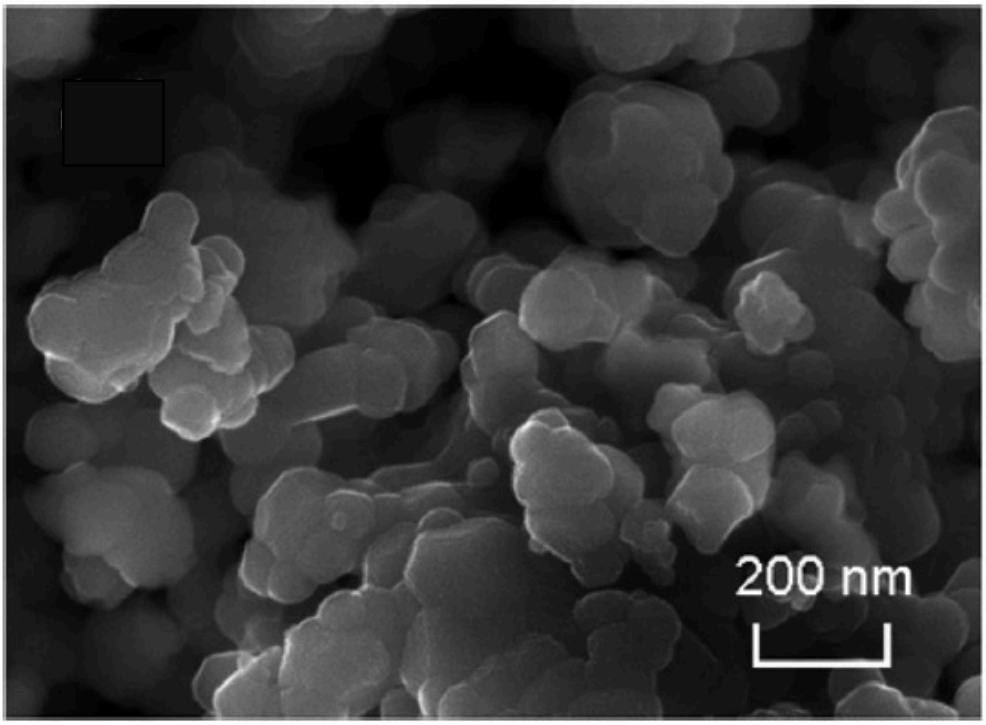

Figure 3.4. FESEM images of the LSCeCrF/GDC cathode fabricated by conventional method [46]. Ref. 46 from American Chemical Society, Copyright 2019.

3.3 Electrochemical performance

The electrochemical measurements of SOECs using infiltrated LSCeCrF/GDC composite cathodes were conducted at 850 °C. The polarization curves (IV curves) of SOECs in the atmospheres of mixture of CO_2 and CO (7:3), and pure CO_2 at various voltages from OCV to 1.85 V were recorded respectively and are shown in Figure 3.5. The IV curve of SOEC with LSCeCrF cathode catalyst fabricated by conventional method (LSCeCrF/GDC-C) in the atmosphere of mixture gas was used for comparison [46]. It can be seen from Figure 3.5 that the current density of the cell with LSCeCrF/GDC cathode fabricated via infiltration can reach 1.59 A cm^{-2} at 1.85 V, which is 42% higher than that of cell with LSCeCrF/GDC cathode through conventional method (1.12 A cm^{-2}). It indicates that infiltration method can effectively improve the performance of the catalyst for CO_2 reduction by efficiently increasing the active reaction areas. The current density of the cell with infiltrated LSCeCrF cathode improved to 1.68 A cm^{-2} in pure CO_2 at 1.85 V due to the higher CO_2 partial pressure and the easier CO_2 adsorption/desorption process [14, 76].

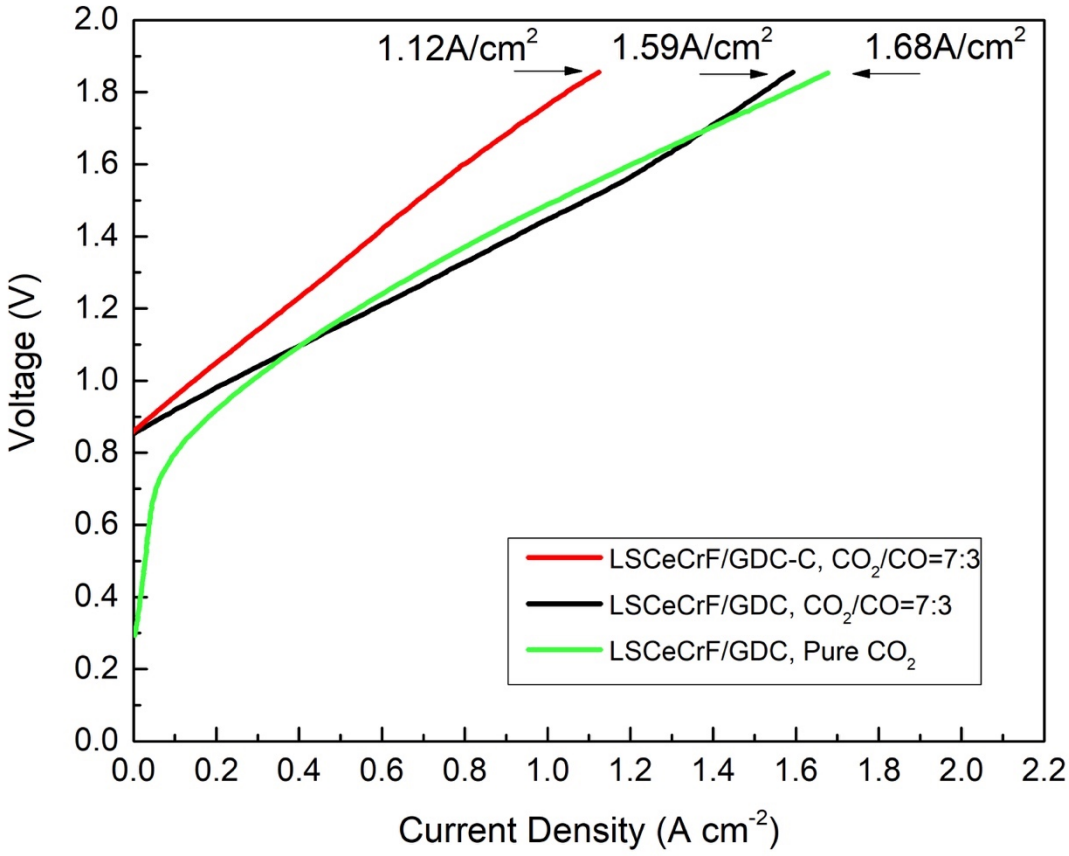

Figure 3.5. IV curves of LSCeCrF+GDC/YSZ/LSCF+GDC at 850 °C through conventional method and infiltration method in the atmosphere of mixture of CO_2 and CO (7:3) and pure CO_2.

The SOEC with infiltrated LSCeCrF cathode was further investigated regarding the short-term performance of CO_2 electrolysis, Faraday efficiency, and CO production at different applied voltages in the atmosphere of mixture of CO_2 and CO (7:3), and the results are shown in Figure 3.6. As the direct CO_2 electrolyzation occurs at voltages above 1V at 850 °C [77], the range of voltage was set from 1.2 to 1.8 V in this work. It can be seen from Fig. 3.6 (a) that the current densities of the SOEC increase in step with the increase of applied voltages. The performance declines somewhat at the initial stage of every step; also, as the applied voltage increases, current

density drops more sharply, and it takes longer time to reach the steady state. It might be caused by the concentration polarization at high overpotentials due to the fast CO_2 consumption and CO formation, leading to the starvation of CO_2 at reaction sites [13]. The current densities, and outlet gas flow rates and compositions were measured to calculate Faraday efficiency and CO production. It is shown that Faraday efficiencies remain at around 95%. The CO production increases significantly, as the applied voltage increases and reaches 8.1 mL min^{-1} cm^{-2} at 1.8V. Compared with the previous works using LSCeCrF/GDC composite cathode fabricated through conventional method, current densities all experienced a degradation in the short-term stability test. But under the same voltages, the current densities from the infiltrated LSCeCrF cathode after stabilized are still much higher than that using conventional method. Regarding the CO production rate and Faraday efficiency, the conventional fabricated SOEC can only reach the CO production rate of about 4.5 mL min^{-1} cm^{-2} at 1.8V, and the Faraday efficiencies are between 60% and 80%, which are all far below than that fabricated by infiltration [46]. The high Faraday efficiency and CO production rate indicate the remarkable catalytic activity of infiltrated LSCeCrF for the direct CO_2 electrolysis at high temperature.

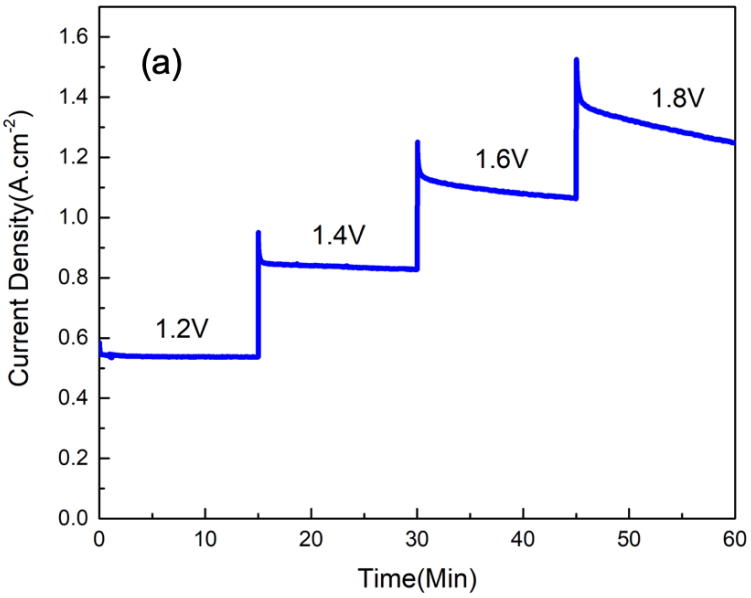

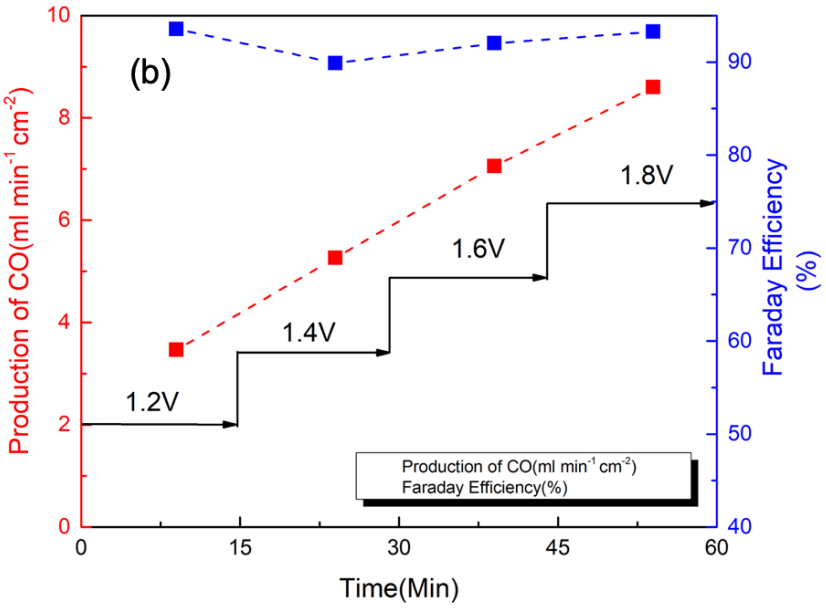

Figure 3.6. (a) Short-term performance of CO2 electrolysis; and (b) Faraday efficiency and CO production for the SOEC with LSCeCrF/GDC cathode at different applied voltages in the atmosphere of mixture CO_2 and CO (7:3) at 850 °C.

The long-term stability was also studied for the LSCeCrF/GDC cathode. As in the 15 min stability test, obvious current density drops can be observed from 1.6 V. The applied voltage of 1.4 V was chosen to perform the stability test initially. As shown in Figure 3.7, the SOEC experienced a degradation with the rate at 5.6×10^{-3} A cm^{-2} $h^{-1,}$ and there was no plateau observed. Comparing with measured stability in Yaqian et al.'s work, the SOEC fabricated by conventional method only has a slightly current density drop at the first hour and then became stable in the rest time in a 24 hours stability test at voltage of 0.7 V vs. OCV (~1.56 V) as shown in Figure 3.8 [46]. Although after the same time at a lower voltage, the current density of LSCeCrF/GDC is still higher than that of LSCeCrF/GDC-C, the faster degradation rate would result in the lower current density after long term operation. Also, the slow reaction rate on CO_2 reduction at such a current density at 1.4 V normally accompanies low catalyst degradation rate. Thus, the stability for the infiltrated LSCeCrF cathode is not satisfying. The infiltrated precursor solution is easier to percolate the porous GDC buffer layer to react with YSZ electrolyte, resulting in the performance degradation [78, 79]. Although infiltration can effectively improve the electrochemical performance of SOEC by increasing specific active area, the stability of electrodes becomes to another problem which needs to be further studied.

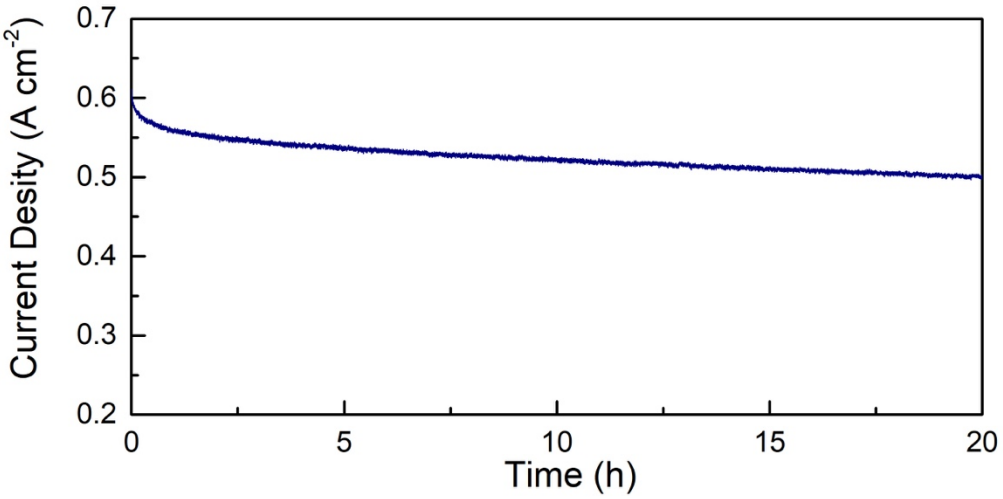

Figure 3.7. 20 hours stability of the SOEC with infiltrated Ni-LSCeCrF/GDC cathode at 850 °C and 1.4 V under the atmosphere of mixture of CO_2 and CO (7:3).

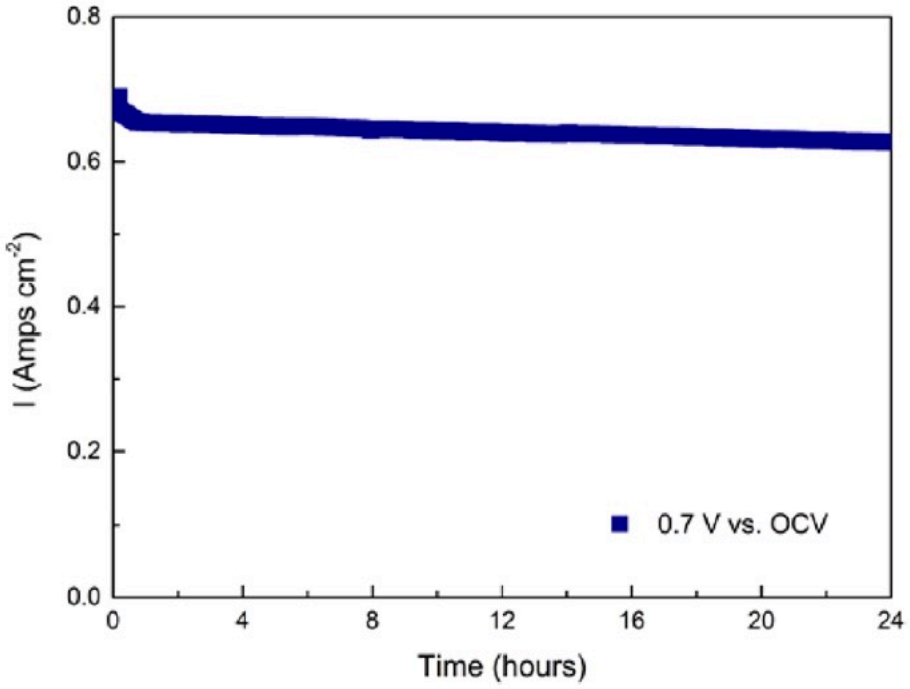

Figure 3.8. 24-hour stability based on LSCeCrF cathode fabricated by conventional method at 850° C and applied voltage of ~1.56 V [46]. Ref. 46 from American Chemical Society, Copyright 2019.

Chapter 4 Microstructure Optimization through Infiltration and In-situ Exsolution of Ni-LSCeCrF

Metallic catalyst Ni has superior catalytic activity for CO_2 reduction and excellent electronic conductivity compared to the perovskite oxide. However, the metallic materials face the agglomeration issue in the atmosphere of CO_2 under high temperature operation. In-situ exsolution combining with infiltration is introduced to further increase catalyst active specific area and improve stability by the exsolution of nano-socket metallic particles. The contents of exsolved NPs were proved by STEM-EDX and DFT calculations. It was also found that exsolved NPs are evenly distributed with similar diameter, and the SOEC with cathode fabricated by infiltration and in situ exsolution has significantly improved electrochemical performance. Moreover, various durability tests were conducted to improve the long term stability for the SOEC.

4.1 Phase and Morphology Analysis

Figure 4.1 shows the XRD patterns of the as-prepared Ni-LSCeCrF powder. The same material formation process that used for LSCeCrF was applied for Ni-LSCeCrF. As shown in Figure 4.1, after sintering in air at 900 °C for 4 hours, the impurity peaks, $SrCrO_4$ (00-001-0698), can be observed in the perovskite phase pattern. After the reduction in hydrogen at 900 °C for 6 h, the minor phase $SrCrO_4$ was dissolved in as-prepared Ni-LSCeCrF in the reduction atmosphere, and a single perovskite oxide structure was obtained, while a small peak at about 52 ° appeared. Based on the material composition, the small peak at ~52 ° could be either Ni or Ni-Fe alloy, which needs to be further verified. It is proved that the hydrogen treatment can not only help to form the

single phase of perovskite structure at a lower temperature, but also be able to actuate the metallic NPs in situ exsolution at the same time.

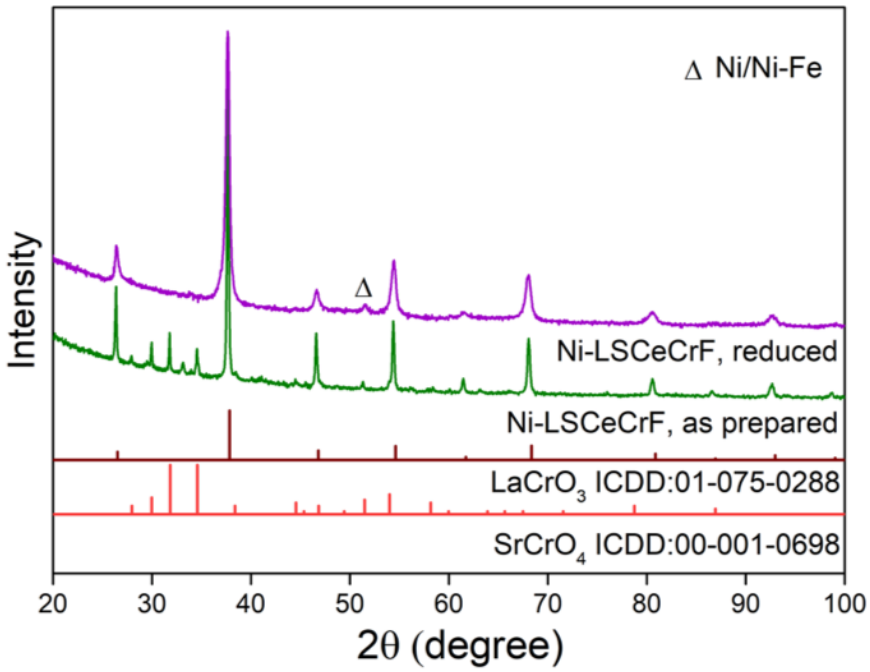

Figure 4.1. XRD patterns of the as-prepared and reduced Ni-LSCeCrF.

To facilitate the observation of metallic NPs exsolution, a Ni-LSCeCrF pellet was prepared and sintered at 1200 °C in air, followed by treatment in H_2 at 900 °C. The pellet surface before and after reduction treatment was characterized by FESEM, and the results are shown in Figure 4.2. The Ni-LSCeCrF grains after sintering in air are smooth without any second-phase NPs on the surface, as shown in Figure 4.2 (a). After hydrogen treatment, many NPs can be observed on the surface of the pellet, which means metallic NPs were exsolved from the Ni-LSCeCrF lattice, as shown in Figure 4.2 (b). The exsolved NPs are uniformly distributed and the particle sizes are similar. The FESEM results indicate that the active metallic NPs can be successfully exsolved

from the parent A-site deficient Ni-LSCeCrF perovskite structure with the uniform size and even distribution. The FESEM images were also taken for the cathode cross-section with infiltrated Ni-LSCeCrF. However, the exsolved Ni-Fe alloy NPs, which are proved by the EDX elemental mapping, are invisible due to their small particle size and the resolution limit of the FESEM image; thus, the obtained image is similar with that of the cathode with infiltrated LSCeCrF. To conclude, through infiltration and in situ exsolution, the microstructural optimized porous cathode with extended TPB areas as well as a new functional catalyst layer generated with very fine and evenly distributed active Ni-Fe metallic nanoparticles possessing satisfying catalytic activity can be fabricated.

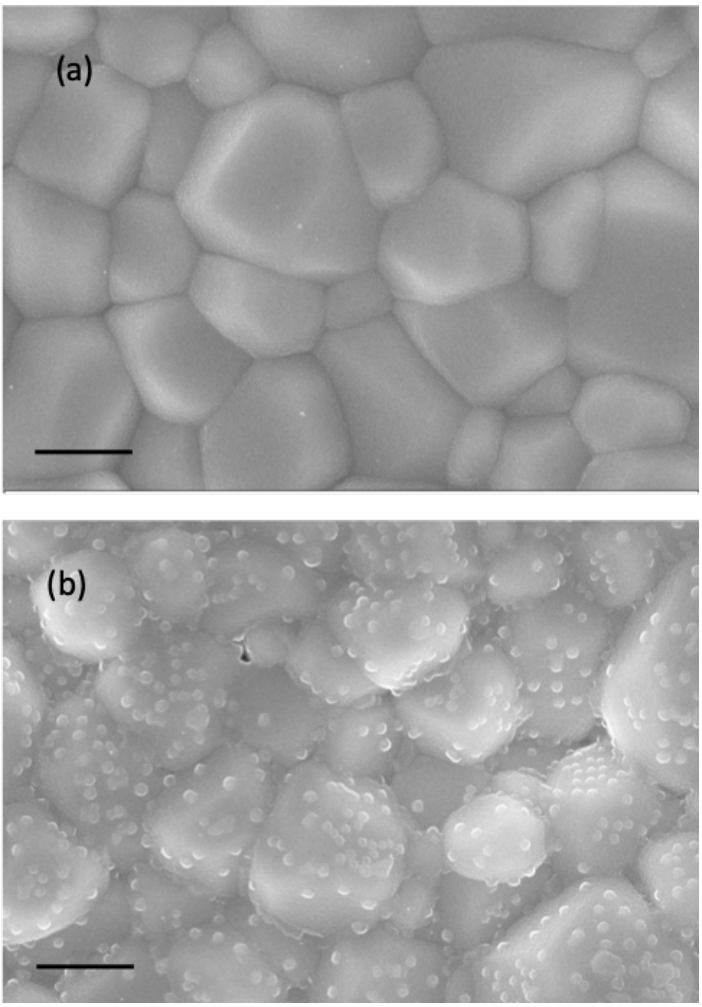

Figure 4.2. FESEM images of the Ni-LSCeCrF pellet (a) before and (b) after reduction (scale bar, 500 nm)

The interface between parent perovskite and exsolved metallic particles was investigated using high-angle annular dark field (HAADF) STEM imaging, and EDX elemental mapping under STEM mode, as shown in Figure 4.3 (a). Good contact was formed at the interface of two particles with the exsolved NP anchored on the surface of the perovskite grain. It can be seen from the interface that the particle exsolved is partially merged into the perovskite oxide structure with an oblate spheroid. Also, the diffusion between the two particles might occur due to the fact that the metallic NPs are directly grown from the perovskite structure, which will further enhance the adhesion between two phases. The interface formed from the in situ exsolution is different from the interface when directly depositing metallic nanoparticles into the perovskite structure, as illustrated in Figure 4.3 (b). Different from the embedded exsolved NPs, the particles that are conventionally deposited has no overlap between two particles, representing a smaller interaction between different phases. Thus, the active metallic NPs grown from in-situ exsolution has improved anchorage against the moves of NPs [80]. The composition of exsolved NP was verified by the EDX elemental mapping. It is obvious that the in-situ exsolved NP has the even Ni and Fe distribution, while the uniform distribution of La, Sr, Ce, Cr, Fe, and O occurs in the parent perovskite particle. It demonstrates that the active metallic NPs compose of the Ni-Fe alloy and are well bonded to the perovskite surface. The strong metal and oxide interface lead to the improved stability by avoiding aggregation of metal NPs as well as coking issue during operation [81, 82].

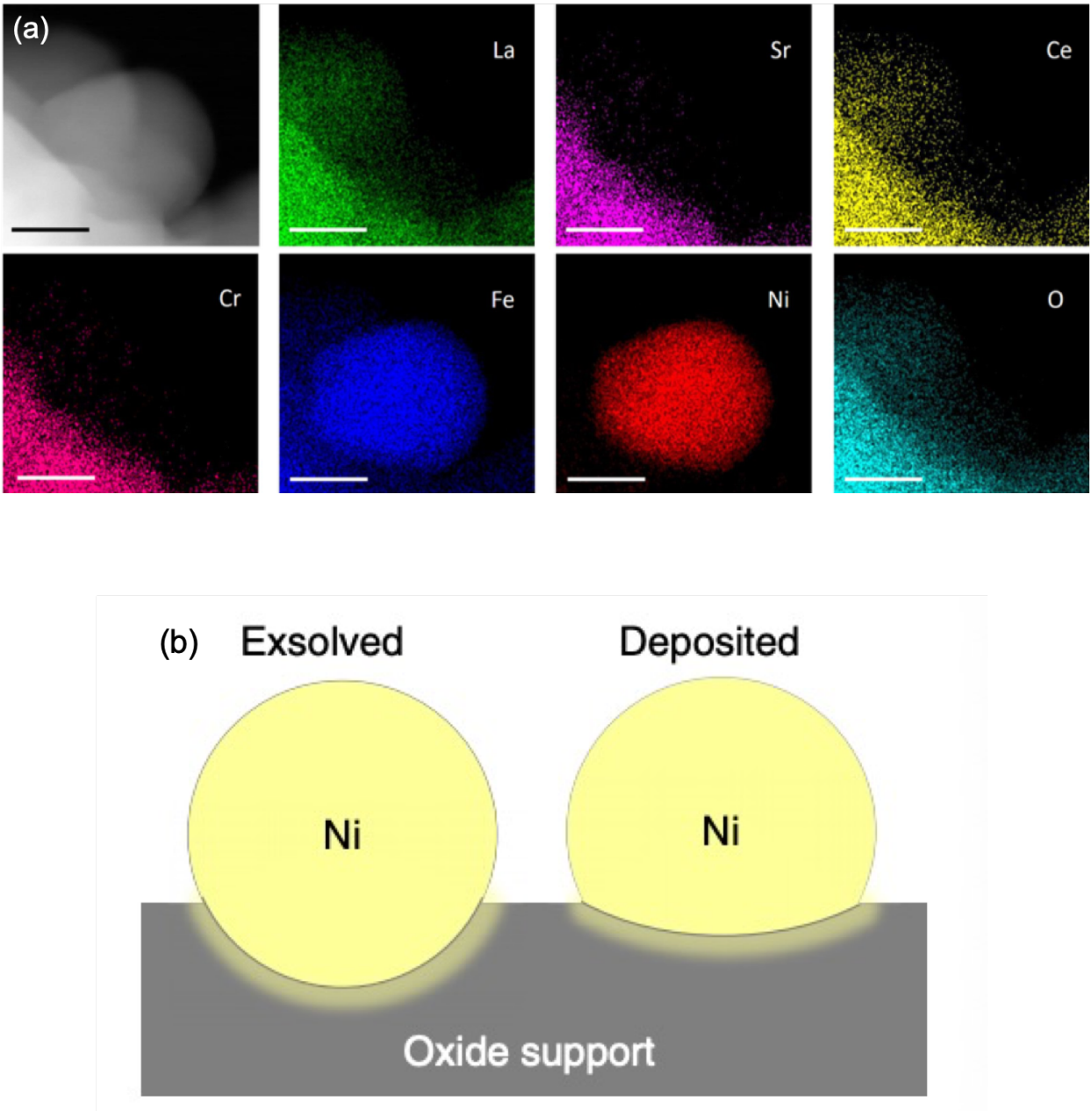

Figure 4.3. (a) High angle annular dark field (HAADF) image of Ni-LSCeCrF with the EDX elemental mapping (scale bar, 30 nm); (b) Schematic diagram of the difference between in-situ exsolution and directly deposition of metallic NP [80]. Ref. 80 from Springer Nature Publishing, Copyright 2019.

EDX-line scanning was also applied to verify the exsolution of Ni and Fe NPs, and the results are shown in Figure 4.4. The horizontal line in Figure 4.4 (a) is the position where the samples were analyzed through line scanning. As we can see, on the left side of the image where

no exsolved NPs observed, lines representing La, Sr, Ce, Cr, Fe have peaks while no peaks on behalf of Ni found. On the right side near the exsolved particles, Ni and Fe peaks occurred, illustrating the exsolution of Ni, and partially Fe. Also, element Ni and Fe can be detected in the parent perovskite oxide structure near the interface, indicating that the metallic NP is submerged into the parent structure. Line scanning has a direct advantage compared with the EDX mapping, which is the direct quantitively analysis of elements distribution regarding the signal intensities, as shown in Figure 4.4 (b). At the position where the NP is embedded into the parent structure, it can be observed that the amount of Ni and Fe increases gradually while the number of other elements decreased, proving that the elements in two phases have inter-diffusion to strength the interact as mentioned above.

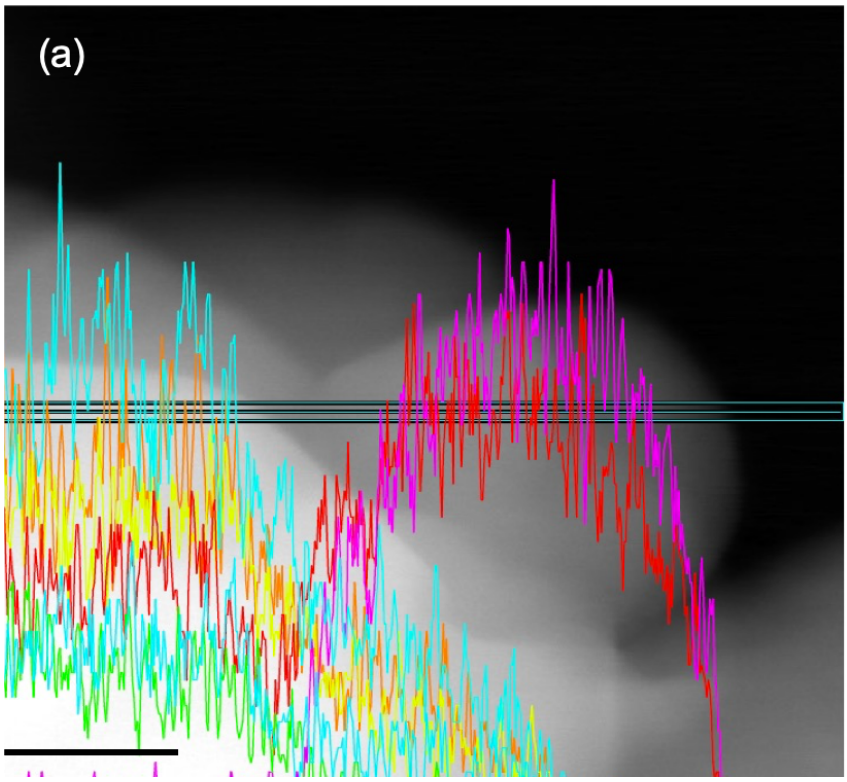

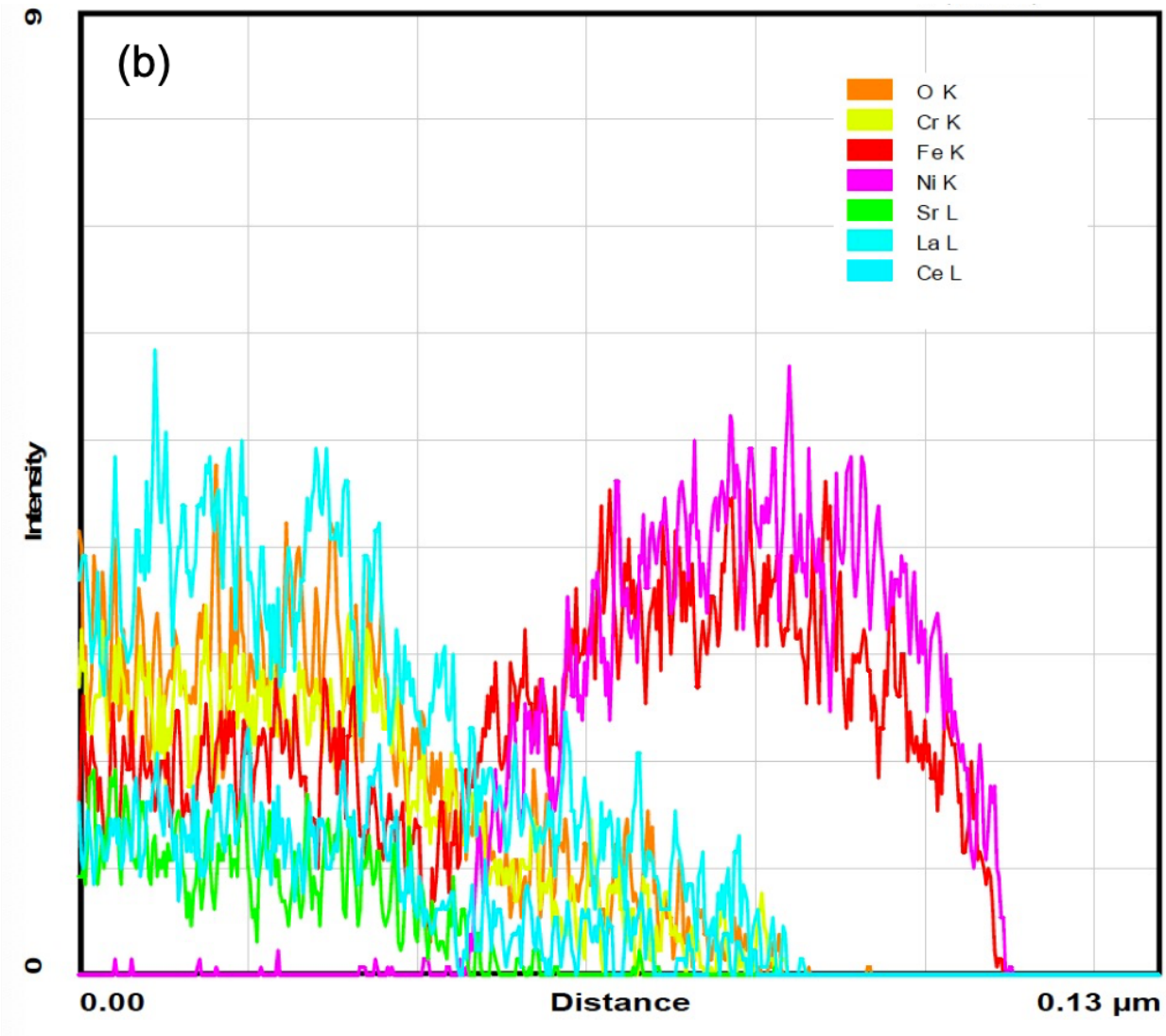

Figure 4.4. Line Scanning of Ni-LSCeCrF through STEM-EDX (a) Overlay of the line scanning result and HAADF image (scale bar: 30 nm); (b) The intensity of element signals vs. distance.

Figure 4.5 shows an overview of the metallic nanoparticles exsolution distribution from the whole sample. The HAADF image of the sample is shown in Figure 4.5 (a). It can be seen that although efforts have been put to make the sample as thin as possible to be suitable for STEM, the different parts still have various thickness, where some exsolved particles are hide in the deeper location. The distribution of Ni and Fe indicates that Ni has almost completely exsolved from the

parent perovskite phase, while only a part of Fe exsolves out of the perovskite lattice at the surface from Figure 4.5 (b) and (c) [83].

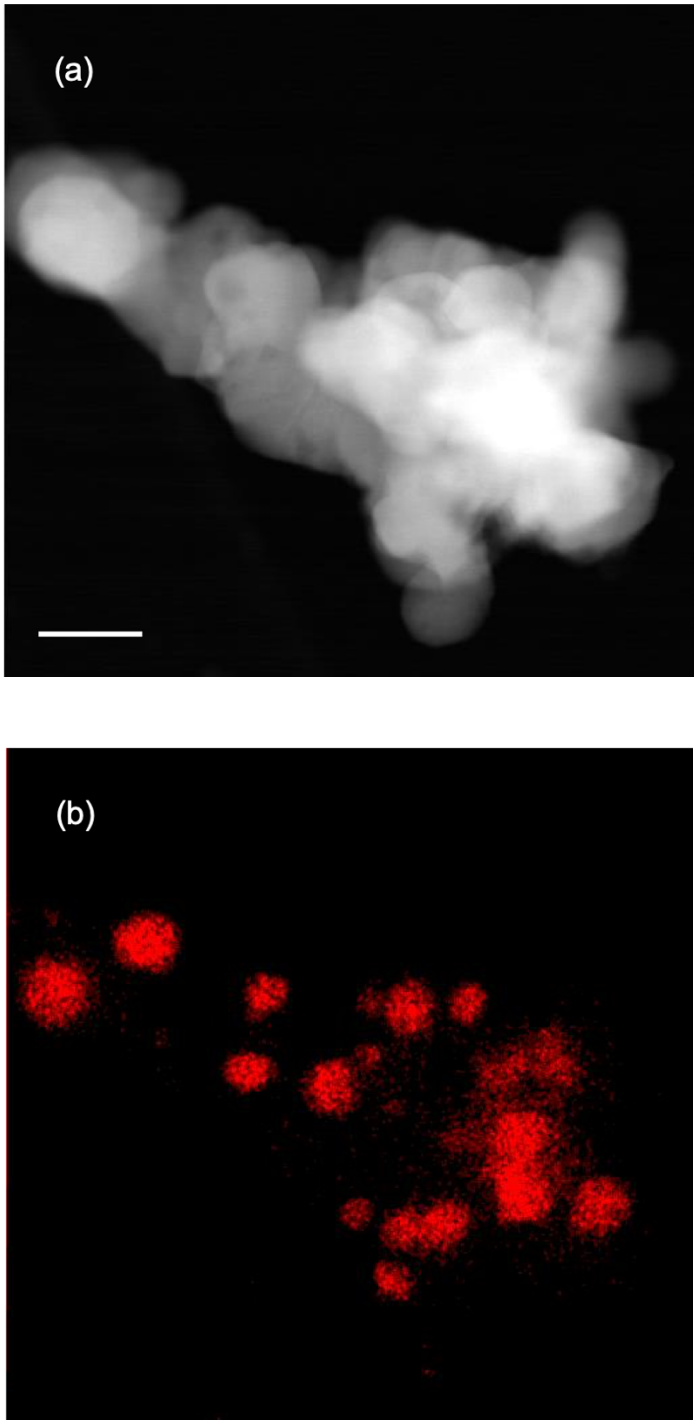

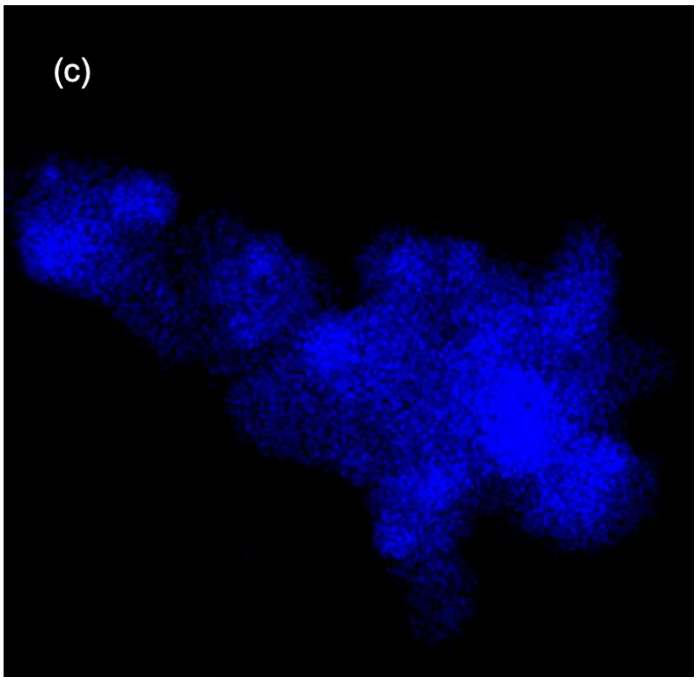

Figure 4.5 (a) HAADF of Ni-LSCeCrF with the EDX elemental mapping of (b) Ni and (c) Fe (scale bar, 100 nm);

4.2 Density Function Theory Calculation

It is reported that the destabilized A-site deficient perovskite structure would induce large amount of oxygen vacancies and promote exsolution of B-site cations [64, 84]. Ni exsolution from perovskite materials has been observed by many researchers while the Fe exsolution has been rarely reported [61, 85, 86]. Kwon *et al.* [87] incorporated theoretical calculations with experimental characterizations to investigate the exsolution behaviors of different transition metals in a perovskite lattice. They found that Fe is unable to exsolve from the perovskite lattice because it requires much higher segregation energy. However, Ni and Fe co-segregation occurs in this work. We carried out theoretical calculations by adopting the segregation mechanism proposed by Kwon *et al.* [87] to reveal the Ni and Fe exsolution behavior in the Ni-LSCeCrF perovskite. The B-site metal (Ni or Fe) firstly segregates with oxygen vacancies from the bulk to the surface and then

experiences the phase transition from metal oxide to metallic phase. In order to discover the effect of doped Ni element on enhancing exsolution of Fe element, we compared the segregation energy of B-site metal and oxygen vacancies between the non-doped perovskite and Ni-doped perovskite. The schematic representation of the segregation mechanism is shown in Figure 4.6.

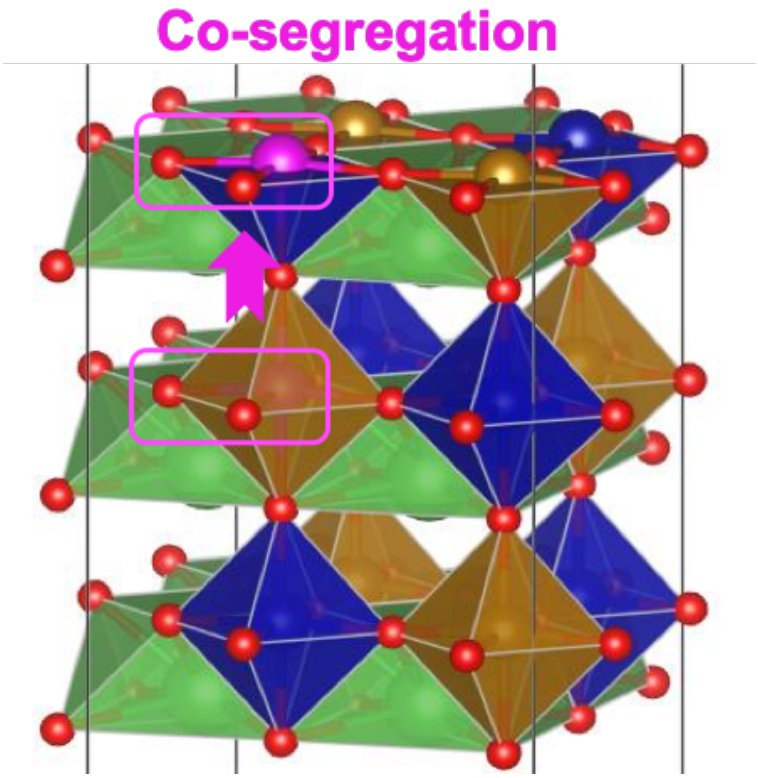

Figure 4.6. Schematic representation of exsolution of B-site cation (Green: La, Blue: Cr, Yellow: Fe, Red: O, Purple: Dopant)

The theoretical calculations were carried out by performing density functional theory (DFT) calculations using Vienna ab initio Simulation Package (VASP) [69, 70]. To facilitate the calculations and focus on the exsolution trends of B-site metals, the LSCeCrF was simplified as $LCr_{0.5}Fe_{0.5}O_3$ (LCFO) in the DFT calculations. The Perdew–Burke–Ernzerhof (PBE) functional based on generalized gradient approximation (GGA) was used to treat the exchange-correlation

energies [88]. Within the projector augmented wave (PAW) framework, the plane-wave cutoff energy was set to 500 eV. A $4\times4\times1$ Monkhorst–Pack k-point sampling of the Brillouin zone was used for the slab model calculation [89]. To determine the partial occupancies, Gaussian smearing was used with a width of 0.05 eV. The forces on atoms and energies were converged to 10^{-5} eV and 0.03 eV $Å^{-1}$ for geometric and electronic optimization. The GGA+U method is applied to consider the on-site Coulomb and exchange interaction with 4, 6.4 and 3.5 to Fe, Ni and Cr [90]. The LCrFO has the space group of Pm-3m with lattice parameters of a=b=c=7.7935 Å as calculated. A six-layered periodic slab model of (001) surface of LCFO was used for the surface simulation, while the two layers are fixed to the bulk geometry and other atoms in the top four layers are fully relaxed during optimization. The thickness of vacuum is 20 Å and constructed along c direction to avoid the interactions between slabs.

According to the influence of oxygen vacancies on facilitating exsolution, it is assumed that the formation of oxygen vacancies in the bulk occurs near the B-site metal before the segregation [46, 47]. The formation energy of oxygen vacancy is given as,

$$E_f = E_{O\_v} + \frac{1}{2}E_{O_2} - E_{clean} \quad (1)$$

where E_f is the oxygen vacancy formation energy, E_{O2} is the total energy of one oxygen molecule in the isolated gas phase and E_{O_v} and E_{clean} represent the total energy of the slab with and without oxygen vacancy, respectively. The tested formation energies of different layers for LCFO by DFT calculations are plotted in Figure 4.7, the oxygen vacancy is much preferable to locate in the third layer. Similarly, for the Ni-doped LCFO, the oxygen vacancy formation energy is lowest in the third layer, which is 1.42 eV. It is also shown that the defect formation energy of Ni-doped LCFO

is lower than that of non-doped LCFO, which indicates the oxygen vacancies are much easier to form in LCFNO due to Ni doping.

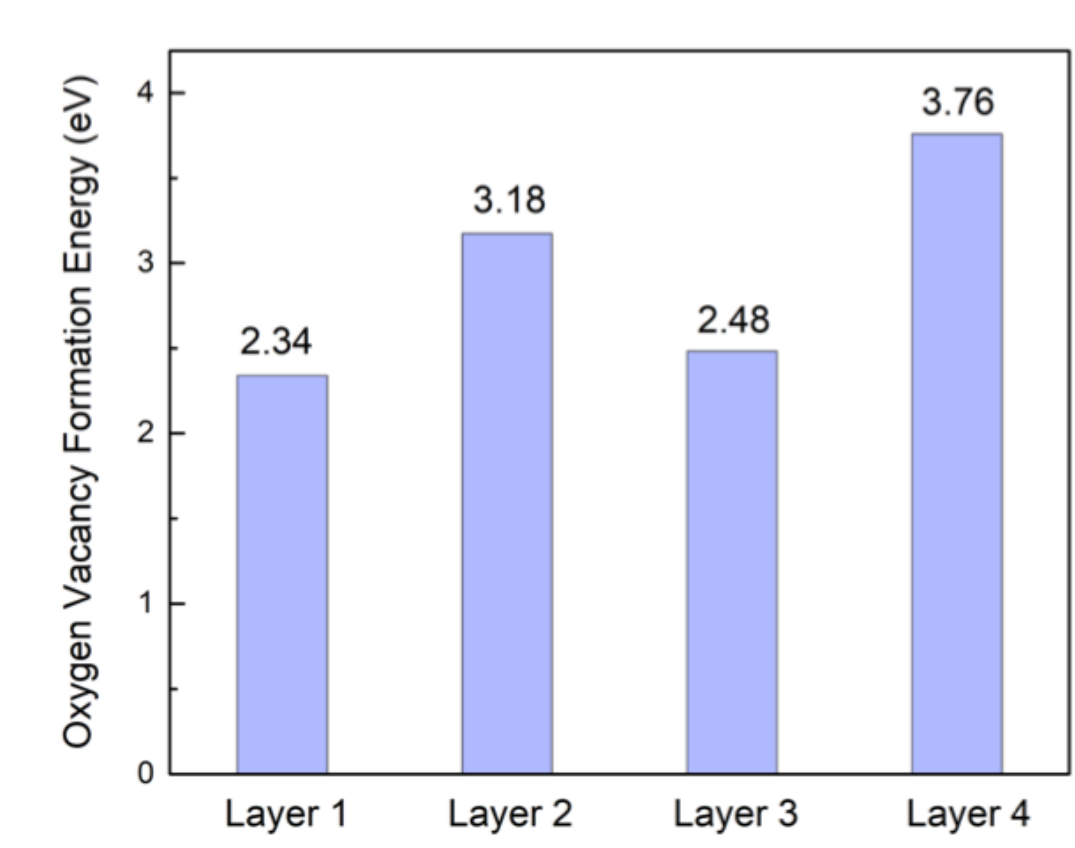

Figure 4.7.Oxygen vacancy formation energies in different layers of LCFO

Based on the speculation of B-site metal exsolution mechanism, the segregation energy is described as the difference of the energies between the B-site metal and its neighboring oxygen vacancies located at the surface and in the bulk phase, which is given as,

$$E_{ex} = E_{B-Ov\_surf} - E_{B-Ov\_bulk} \quad (2)$$

where E_{ex} is the co-segregation energy, and $E_{B\text{-}Ov\_surf}$ and $E_{B\text{-}Ov\_bulk}$ are the energies of after and before B-site metal and the oxygen vacancy segregating, respectively. In Figure 4.8, it can be seen from the calculated segregated energy is 1.95 eV, -0.40 eV and -0.47 eV for Fe exsolution from LCFO and Ni-doped LCFO and Ni exsolution from Ni-doped LCFO. It should be noted that the negative exsolution energy indicates the B-site metal can be easily exsolved from bulk to the surface. We found that without Ni dopant, the segregation energy of Fe is positive, indicating it is hard to exsolve to the surface. Moreover, with Ni doping, both Fe and Ni segregation energies are negative, showing the potential trend of these two types of nanoparticles to form exsolution and is in good agreement with our experimental results.

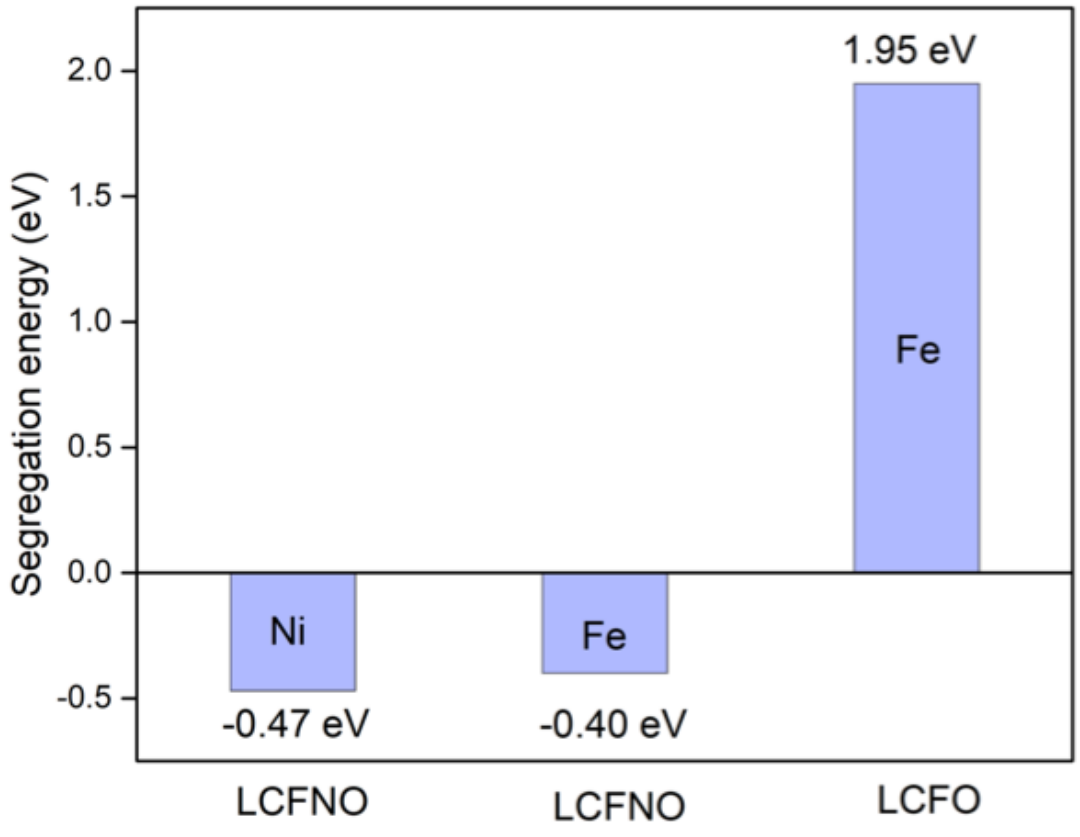

Figure 4.8. Comparison of segregation energy with different transition metals on B-site.

4.3 Electrochemical performance

The electrochemical measurements of SOECs using infiltrated Ni-LSCeCrF/GDC were conducted at 850 °C in the mixed gas and pure CO_2. The IV curves of SOEC at various voltages from OCV to 1.85 V were recorded, respectively, and are shown in Figure 4.9. The IV curves obtained in Chapter 3 are also included for comparison. It can be seen from Figure 4.9 (a) that the SOEC with Ni-LSCeCrF/GDC cathode has the current density at 2.11 A cm^{-2} in mixed gas at 1.85 V, which is about 33% higher than that of LSCeCrF/GDC cathode (1.59 A cm^{-2}) and 88% higher than that of LSCeCrF/GDC-C cathode. From Figure 4.9 (b), the current density of Ni-LSCeCrF/GDC further improved to 2.26 A cm^{-2} in pure CO_2 at 1.85 V, about 35% higher than that of LSCeCrF/GDC cathode (1.68 A cm^{-2}). The change of atmospheres from mixed gas to pure CO_2 can improve current density of about 7% due to the higher CO_2 partial pressure and the faster CO_2 adsorption and desorption, similarly for the LSCeCrF/GDC. The remarkably improved electrochemical catalytic activity of the Ni-LSCeCrF/GDC cathode can be attributed to in-situ exsolution of Ni-Fe bi-metallic NPs socked on the perovskite surface, which significantly extend the active reaction areas[83]. Also, the exsolved Ni-Fe NPs can promote high-temperature chemical adsorption and activation of CO_2 [91].

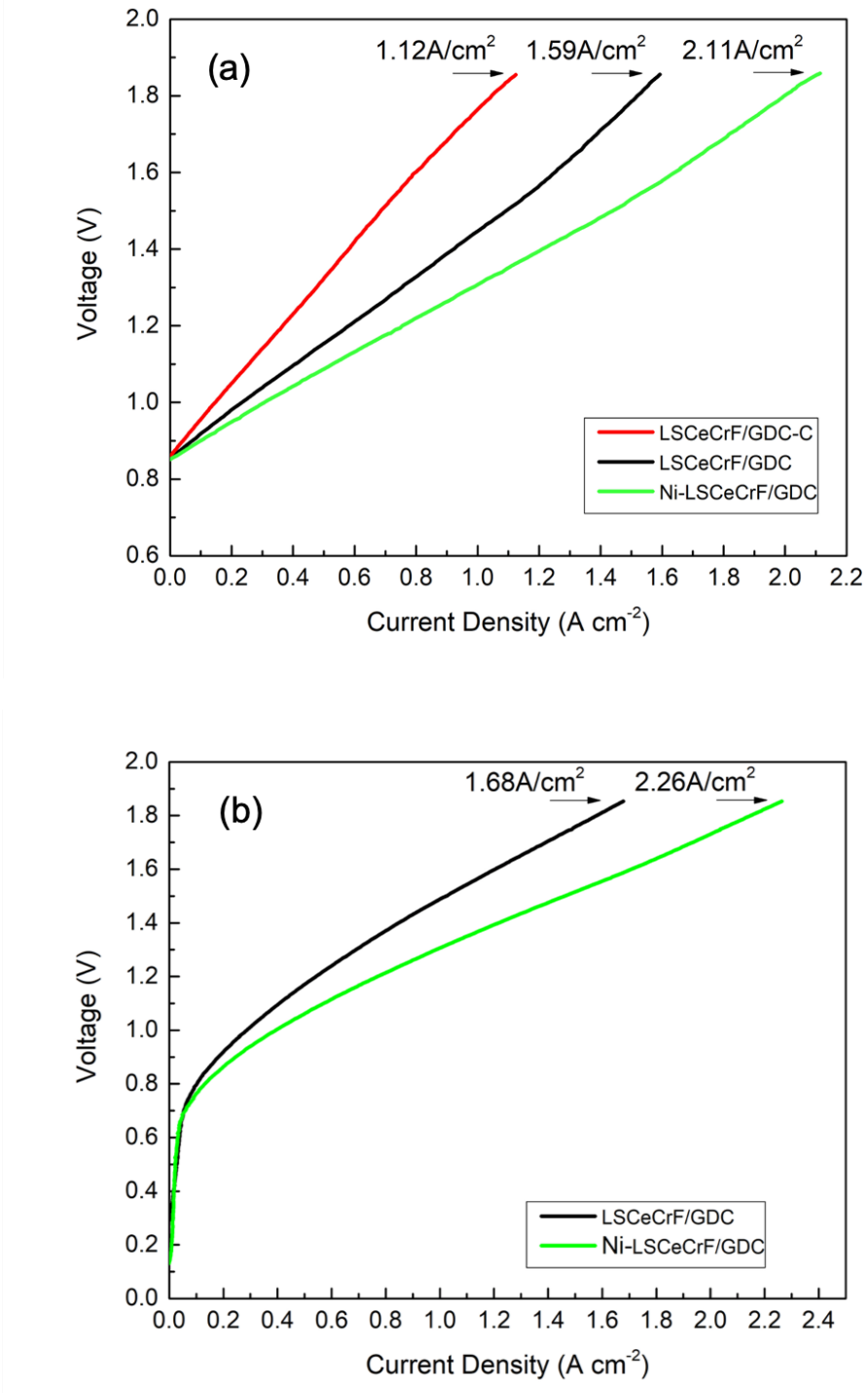

Figure 4.9. IV curves of LSCeCrF+GDC/YSZ/LSCF+GDC and Ni-LSCeCrF +GDC/YSZ/LSCF+GDC at 850 °C (a) through conventional method and infiltration method in the atmosphere of mixture of CO_2 and CO (7:3); (b) through infiltration method in the atmosphere of pure CO_2.

The EIS was applied to study the polarization resistances of cathode fabricated by infiltration of Ni-LSCeCrF in both atmospheres at various applied voltages from OCV to 1.8 V. To simulate the results measured from experiment, an equivalent circuit was designed based on the impedance pattern of the SOEC and used in the software. As shown in Figure 4.10, the equivalent circuit has mainly four parts, an inductive impedance L_1, an ohmic resistance R_s, and two resistances with constant phase elements, R_1CPE_1 and R_2CPE_2, representing the two electrodes [31].

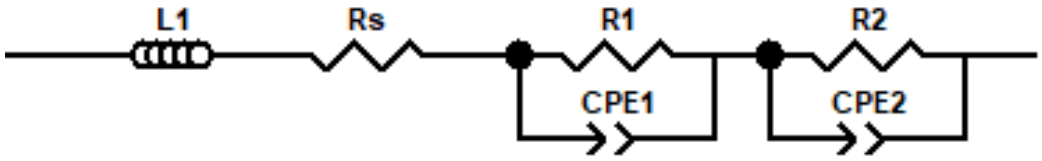

Figure 4.10. Equivalent Circuit for SOEC Ni-LSCeCrF +GDC/YSZ/LSCF+GDC.

The experimental and simulated EIS results of Ni-LSCeCrF +GDC/YSZ/LSCF+GDC at 850 °C, as well as the comparison of polarization resistances in different atmospheres, were shown in Figure 4.11. The ohmic resistance, mainly relative to the resistance of YSZ electrolyte, is a constant value under different applied voltages in both atmospheres due to it is an intrinsic property of the YSZ material as the function of temperature. The polarization resistances were focused in this study so that the constant ohmic resistances were removed from each curve. The change of polarization resistances at the different applied voltages is the reason for changes of total resistance, which is reflected by the slopes in the polarization curves. As we can see from Figure 4.11 (a) and (b), the polarization resistances decreased obviously as the applied voltages increased. However,

the polarization resistance for the SOEC in the atmosphere of pure CO_2 at OCV is extremely large. The reason for this phenomenon is that the OCV is too low (near 0.1 V) compared to the voltage that CO_2 start to react at 850 °C. From Figure 4.11 (c), both R_H and R_L, as well as the total polarization resistance for the measurement in pure CO_2 is lower than that of in mixed gas under low applied voltages. It illustrated that the transportation of charge carriers (represented by R_H), and the adsorption and desorption of reactants, as well as the gas phase diffusion (represented by R_L), are both faster in the mixed gas atmosphere under low voltages [92]. As the voltage increased, both R_H and R_L for the cell tested in pure CO_2 decreased obviously while these in the mixed gas only slightly decreased. Until 1.8 V, these two values became lower for pure CO_2. This result is consistent with the polarization curve, where the current densities are higher in the mixed gas at the beginning and become opposite when voltages are increased. Also, it can be observed that the R_H is dominant in the polarization resistance. The porous cathode with in-situ exsolution of active metallic NPs by the microstructure optimization can ensure the excellent chemisorption of reactants and diffusion of gas, while the electrochemical catalytic activity of perovskite catalyst still has space to be improved.

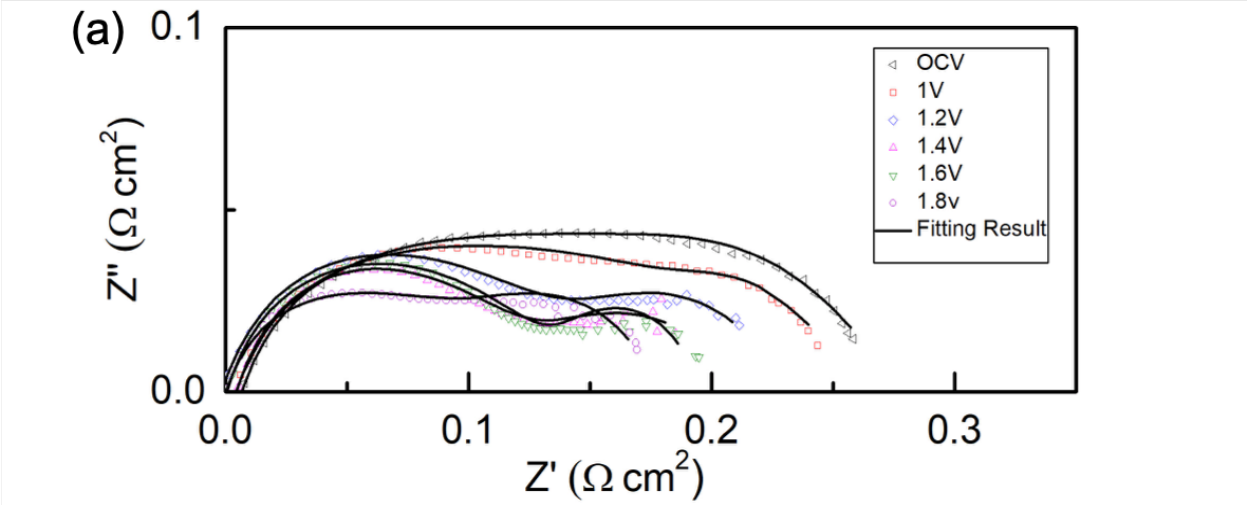

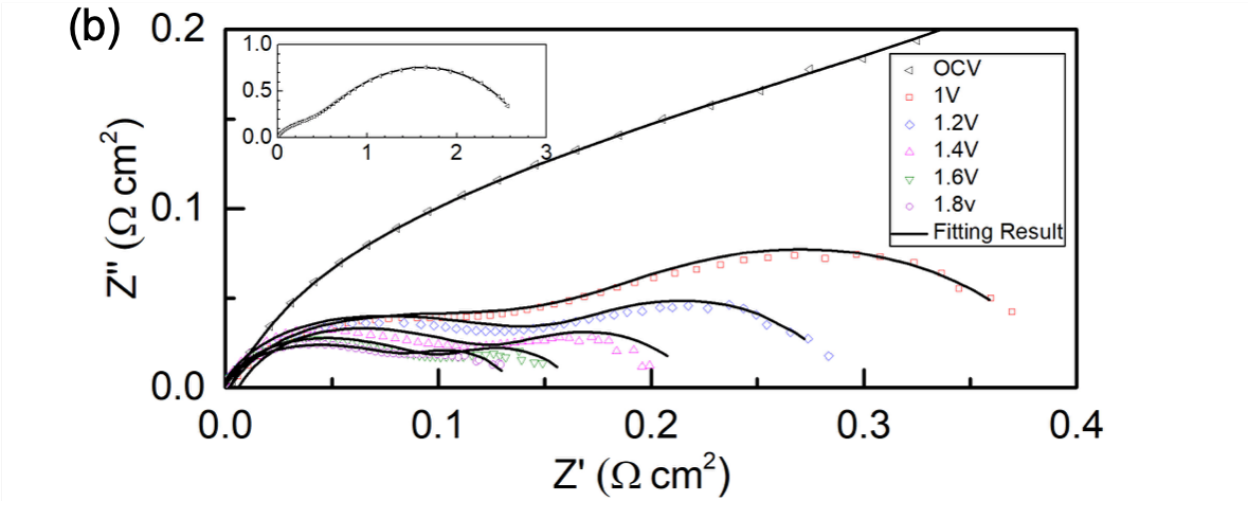
(b)
Z'' (Ω cm²)
Z' (Ω cm²)
OCV
1V
1.2V
1.4V
1.6V
1.8v
Fitting Result

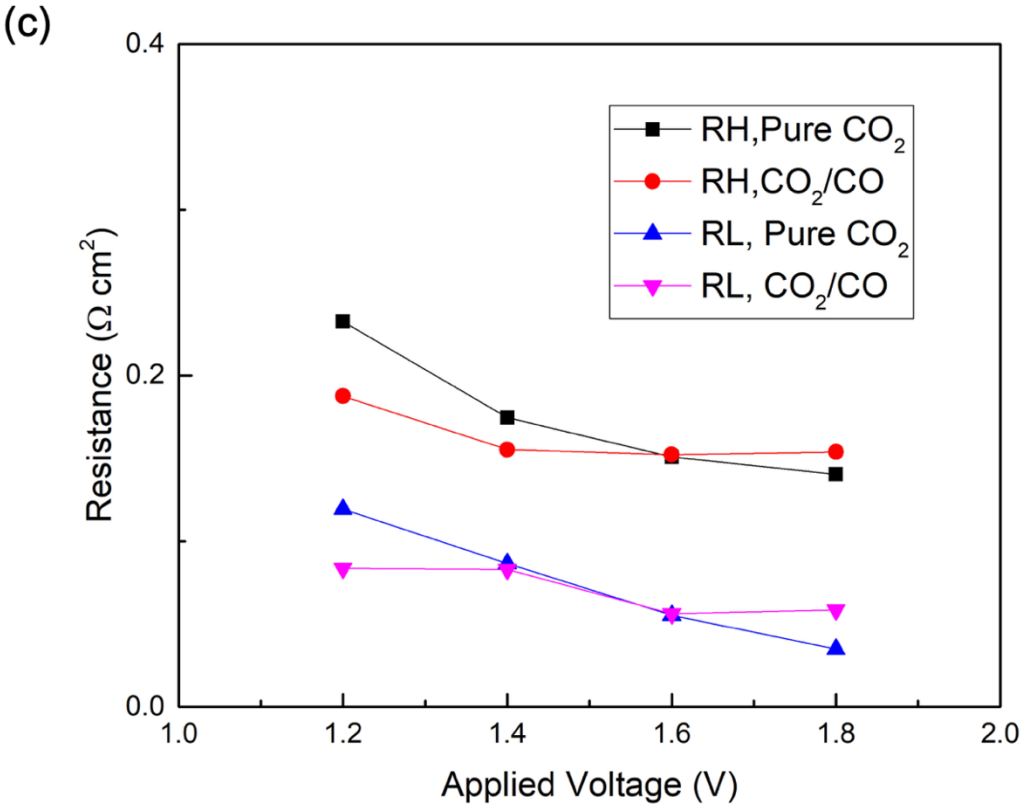
(c)
Resistance (Ω cm²)
Applied Voltage (V)
RH,Pure CO2
RH,CO2/CO
RL, Pure CO2
RL, CO2/CO

Figure 4.11 Experimental and simulated EISs of Ni-LSCeCrF +GDC/YSZ/LSCF+GDC at 850 °C (a) in the atmosphere of mixture of CO_2 and CO (7:3); (b) in the atmosphere of pure CO_2; (c) and the comparison of simulated polarization resistances in two atmospheres.

Short-term performance of CO_2 electrolysis, Faraday efficiency, and CO production at different applied voltages in the atmosphere of mixed gas and pure CO_2 are conducted for the cell with Ni-LSCeCrF cathode. As the performance and stability are better for pure CO_2, the results from pure CO_2 are shown in Figure 4.12. It can be seen from Figure 4.12 (a) that although the performance declines somewhat at the beginning for each voltage, similar to the previous results for infiltrated LSCeCrF, the current density drop slows down rapidly and tends to reach a steady value. A stable current density of 1.8 A cm^{-2} can be reached at 1.8V, which is more stable than that of the SOEC with infiltrated LSCeCrF cathode. The same method as before was used to calculate Faraday efficiency and CO production. It is shown that Faraday efficiencies reach around 90% and remain almost constant at different voltages. The CO production increases significantly as the applied voltage increases and reaches 11.2 mL min^{-1} cm^{-2} at 1.8 V. The above results indicated that the infiltrated perovskite oxide Ni-LSCeCrF with in-situ exsolution of Ni-Fe nanoparticles is a promising potential catalyst for the direct CO_2 reduction at high temperature. Moreover, the Faraday efficiencies which stay constant at around 90% under different voltages can prove that there is no carbon deposition occur during the reaction, indicating the stability of the electrode structure. The increasing CO production can also prove this conclusion.

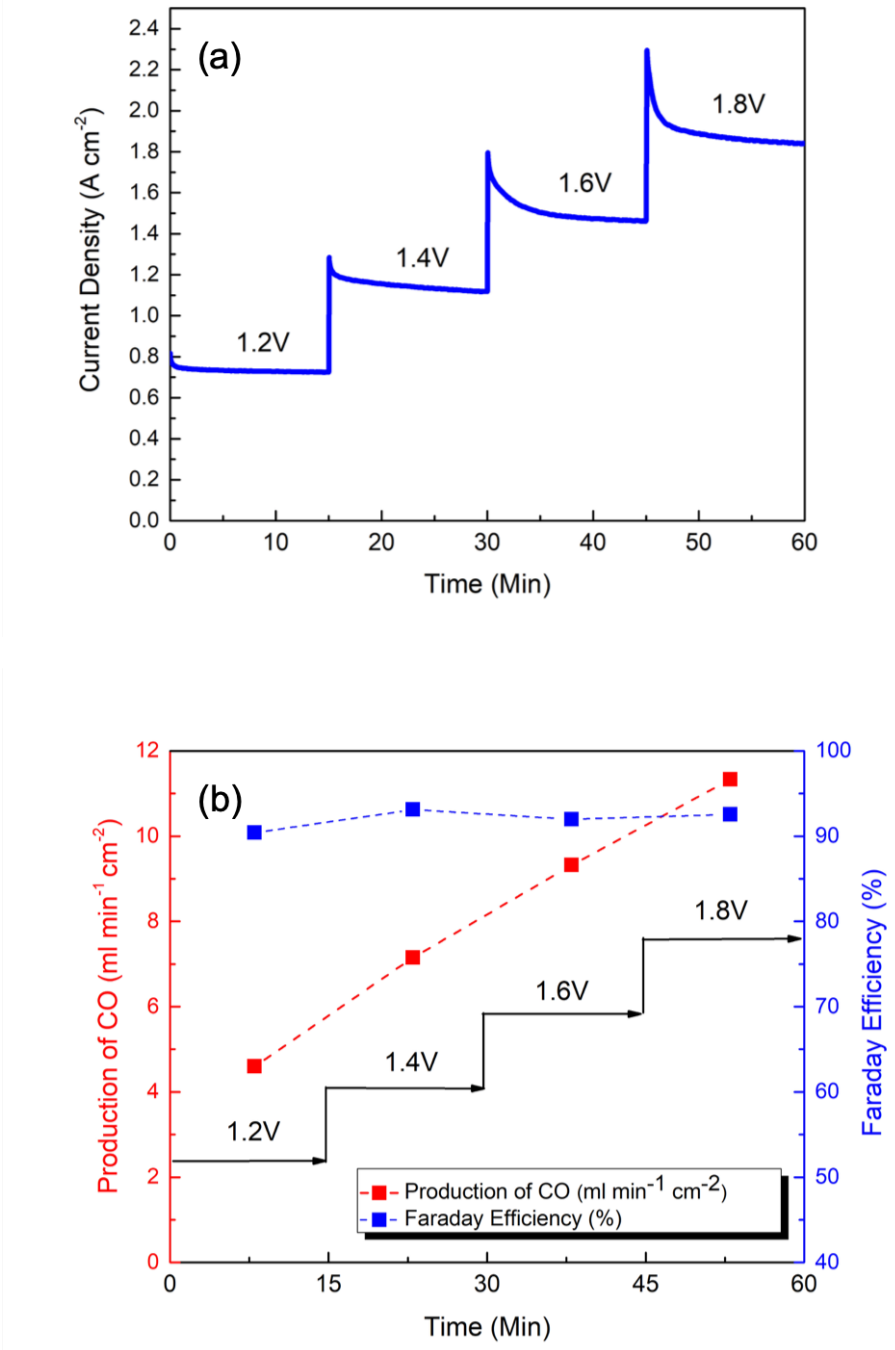

Figure 4.12. (a) Short-term performance of CO_2 electrolysis; and (b) Faraday efficiency and CO production for the SOEC with Ni-LSCeCrF/GDC cathode at different applied voltages in the atmosphere of pure CO_2 at 850 °C.

4.4 Studies on long-term durability

Long-term durability test was performed in the atmosphere of pure CO_2 at 1.6 V for 100 h after several hours of activation to study the stability of SOEC with the Ni-LSCeCrF/GDC cathode. Multiple attempts with different buffer layer structures and temperature were made to find the most stable condition.

The diffusion-block buffer layer was fabricated between LSCF anode according to the method mentioned in Chapter 1.6.3, Buffer layer. The obtained stability test result, as well as the FESEM image of the fabricated buffer layer, are shown in Figure 4.13. The SOEC experienced a degradation rate of 1.78 $\times 10^{-3}$ A cm^{-2} which is still not satisfying and obvious drop can be observed for the stability curve. The corresponding FESEM image in Figure 4.13 (b) shows that the buffer layer is porous, although the two layers can be distinguished. This porous buffer layer cannot block the infiltrated precursor solution, leading to the severe reaction between LSCF and YSZ electrolyte. Multiple productions of GDC powder and buffer layer fabrication following Lee's experiment [51] were attempts, but the buffer layer was still not dense enough.

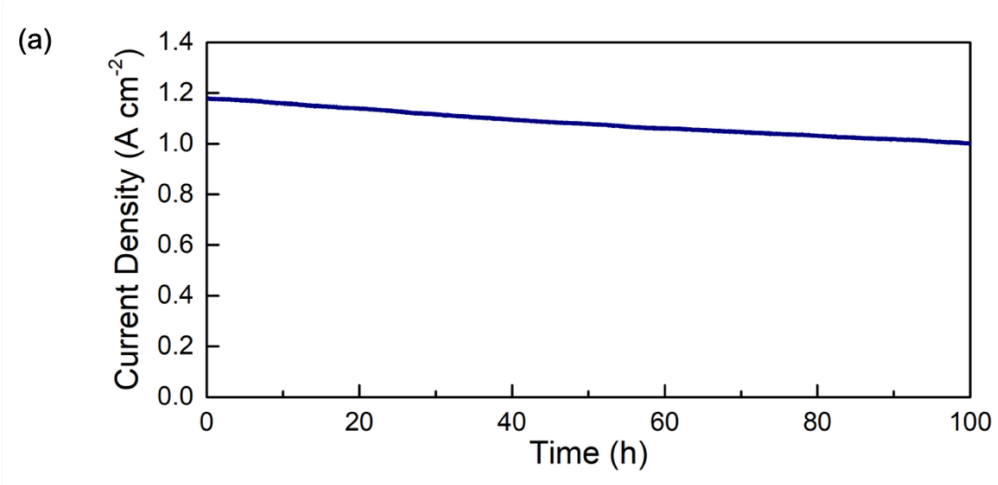

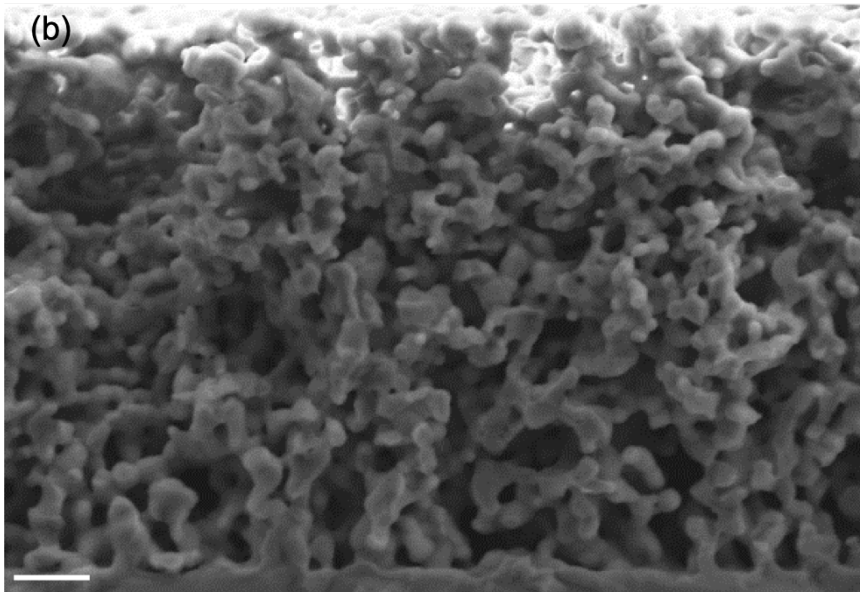

Figure 4.13. (a) Long-term stability of the SOEC with infiltrated Ni-LSCeCrF/GDC cathode at 850 ℃ and 1.6 V under the atmosphere of pure CO_2; (b) FESEM image of corresponding GDC buffer layer fabricated according to Lee et.al's experiment [51] (scale bar: 2μm) .

It is commonly believed that the perovskite cathode material family LSCrX has a stable structure and is compatible with YSZ electrolyte, which means the GDC buffer layer is not required between them [93]. To improve the stability, the buffer layers were screen printed on both sides of electrolyte using the GDC powders with 2% cobalt. As shown in Figure 4.14 (a), the cell experiences slight degradation during the static-voltage operation. The degradation rate is averagely 1.49×10^{-3} A cm^{-2} h^{-1} during the test, and the rate slows down gradually. The current density remains at 1.01 A cm^{-2} after 100 hours stability test, which is still much higher than the previous work using LSCeCrF/GDC-C cathode (0. 65 A cm^{-2} after 24 hours) [46]. Also, with adding of cobalt as sintering aid, the GDC buffer layer became dense with some small pores that

are not interconnected. The improved stability may be caused by the formation of dense buffer layer and the insulation between cathode and electrolyte.

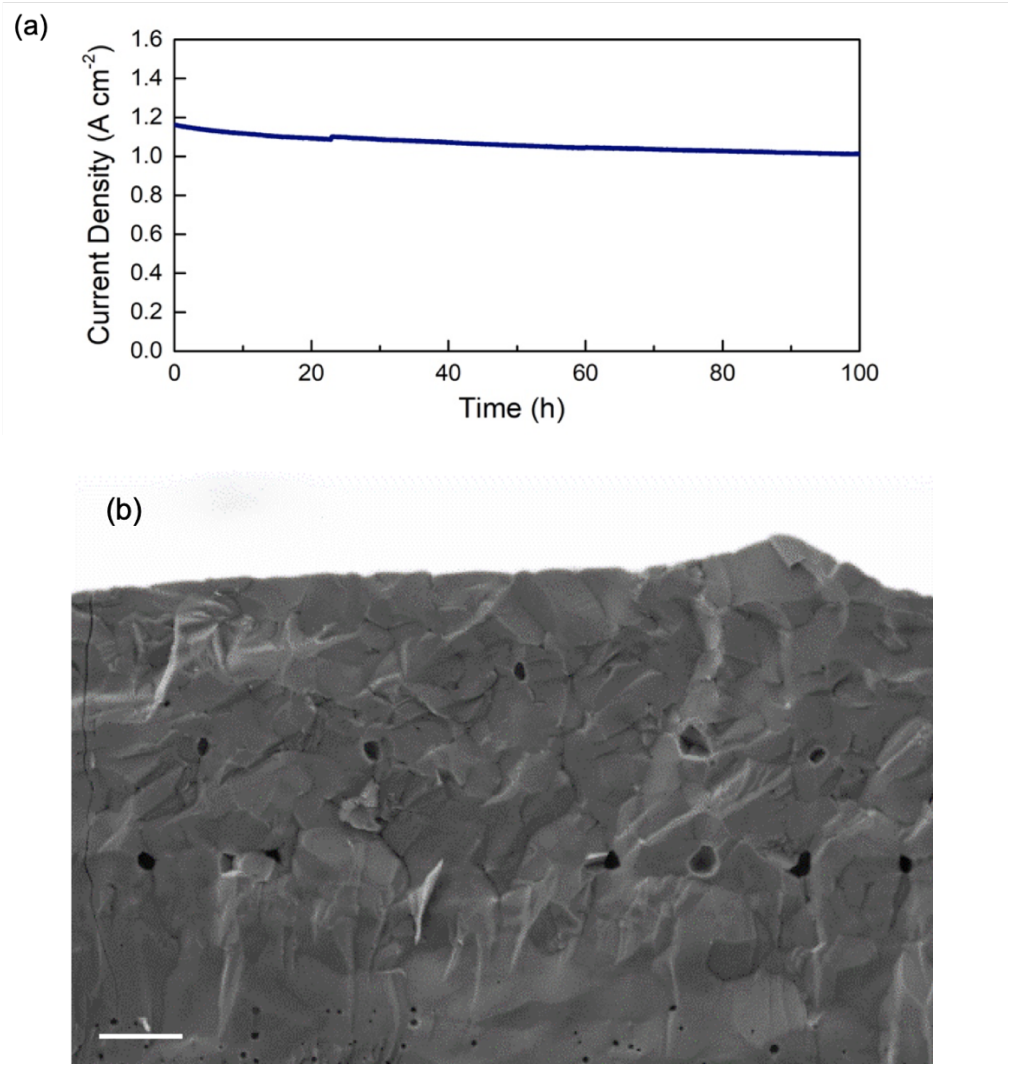

Figure 4.14. Long-term stability of the SOEC with infiltrated Ni-LSCeCrF/GDC cathode at 850 °C and 1.6V under the atmosphere of pure CO2; (b) FESEM image of corresponding buffer layer fabricated on both sides of electrolyte with GDC powder with 2% Co (scale bar: 2μm).

Catalyst has its decay rate depending on the temperature. The influence of temperature on long-term stability was also studied. It was shown in Figure 4.15 (a) that the current density remains almost constant during the 100 h stability test with only 0.5 $\times 10^{-3}$ A cm^{-2} h^{-1} with the

same structure as Figure 4.14 (b). The stability is excellent and satisfying, but another issue showed up, which is the decrease in current density. The current density can only reach 1.62 A cm^{-2} in the atmosphere of pure CO_2 and 1.50 A cm^{-2} in the atmosphere of mixed gas under 1.85 V at 800 °C which are about 20% lower than that at 850 °C. The conductivity of YSZ is very sensitive to the temperature, and even a slight decrease in operation temperature would lead to a significant increase of the ohmic resistance for the cell. It is required to improve the electrochemical performance of SOEC at a lower temperature if we want to maintain stability by decrease the operation temperature.

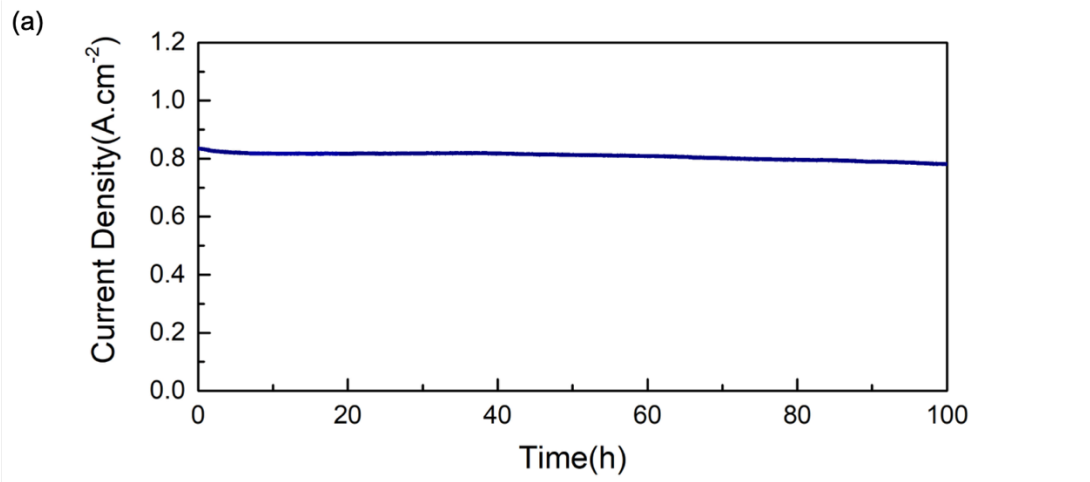

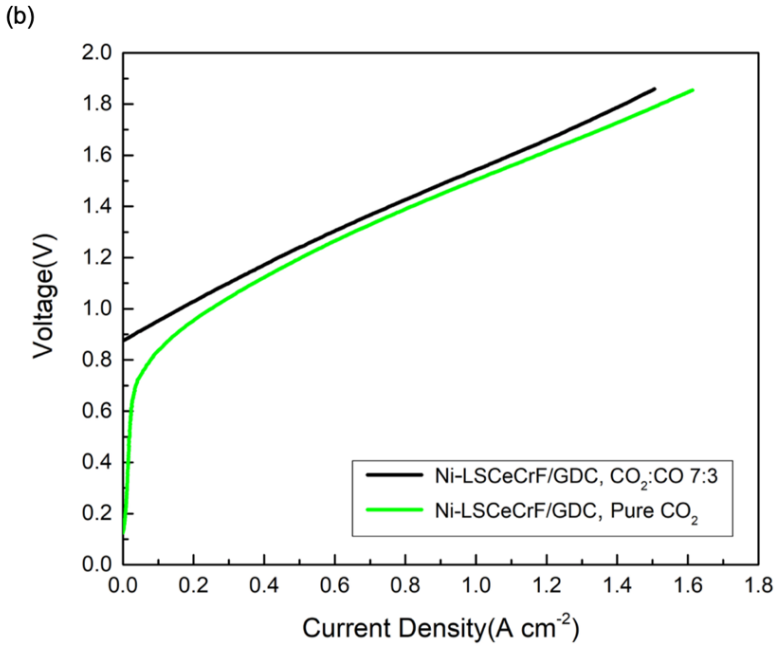

Figure 4.15. Long-term stability of the SOEC with infiltrated Ni-LSCeCrF/GDC cathode at 800 °C and 1.6 V under the atmosphere of pure CO2; (b) IV curves of Ni-LSCeCrF +GDC/YSZ/LSCF+GDC at 800 °C in the atmosphere of mixture of CO_2 and CO (7:3) and pure CO_2.

Chapter 5 Conclusion and Future Work

5.1 Microstructure Optimization through Infiltration of LSCeCrF

In Chapter 3, the cathode microstructures of LSCeCrF were successfully optimized via infiltration method. The following conclusions are drawn:

1. Sintering in air followed by hydrogen treatment can effectively lower the single-phase formation of perovskite structure.
2. Through infiltration, a thin film of catalyst can form on the surface of backbone, resulting in extended triple phase boundary (TPB) and increased active reaction area.
3. The electrochemical performances, regarding the polarization curves, short term stability, CO production rate, and Faraday efficiency, are significantly improved by the optimized microstructure of cathode.
4. The long-term stability was unsatisfying, which required further studies.

5.2 Microstructure Optimization through Infiltration and In-situ Exsolution of Ni-LSCeCrF

In Chapter 4, the Ni-LSCeCrF/GDC nanostructured cathode was fabricated by infiltration and in-situ exsolution of active Ni-Fe alloy nanoparticles. It can be concluded that:

1. The current densities further improved while the exsolution of active metallic NPs occurred.
2. The electrochemical performance of the SOEC measured in pure CO_2 is better compared with that in mixed gas, as shown in the polarization curves and EIS.
3. STEM and EDX proved that the exsolved NPs are well bonded with the parent perovskite structure and the compositions of exsolved NPs are confirmed to be Ni and Fe.

4. The DFT results reveal that Ni doping could reduce the segregation energy of Fe, indicating a new strategy of multiple elements doping to form active alloys by in situ exsolution.
5. Fabrication of buffer layer on both sides of electrolyte using GDC powder consisting 2% cobalt can provide the satisfying stability of SOEC. Decrease in operation temperature should further improve the stability.

5.3 Future Work

The microstructure of cathode can be further optimized using the same material with new fabrication method. Using electrospinning to fibrate the perovskite oxide in the shape of nanofibers is considered in the next stage to increase the active reaction area.

The intrinsic catalytic activity of perovskite oxide can be improved as well. For example, the element Cr in Ni-LSCeCrF has a stabilizing effect on the perovskite structure but with limited catalytic activity. Suitable elements can be selected to substitute Cr element to increase the activity as well as maintain the structure stability.

The cathode supported SOEC structure is a promising way to maintain satisfying electrochemical performance when lowering down the operation temperature. In cathode supported structure, the YSZ electrolyte can be fabricated as thin as possible to decrease the ohmic resistance even at low operation temperature.

References

1. Song, C., *Global challenges and strategies for control, conversion and utilization of CO2 for sustainable development involving energy, catalysis, adsorption and chemical processing.* Catalysis Today, 2006. **115**(1-4): p. 2-32.
2. Boden, T., R. Andres, and G. Marland, *Global, Regional, and National Fossil-Fuel CO2 Emissions (1751-2014)(V. 2017)*. 2017, Carbon Dioxide Information Analysis Center (CDIAC), Oak Ridge National ….
3. *Global Greenhouse Gas Emissions Data*. Available from: https://www.epa.gov/ghgemissions/global-greenhouse-gas-emissions-data#Reference%201.
4. Keeling, R., *Atmospheric CO_2 records from sites in the SIO air sampling network. Trends: A Compendium of Data on Global Change.* http://cdiac. ornl. gov/, 2008.
5. Spinner, N.S., J.A. Vega, and W.E. Mustain, *Recent progress in the electrochemical conversion and utilization of CO2.* Catal. Sci. Technol., 2012. **2**(1): p. 19-28.
6. Martín, A.J., G.O. Larrazábal, and J. Pérez-Ramírez, *Towards sustainable fuels and chemicals through the electrochemical reduction of CO 2: lessons from water electrolysis.* Green Chemistry, 2015. **17**(12): p. 5114-5130.
7. Zheng, Y., et al., *A review of high temperature co-electrolysis of H2O and CO2 to produce sustainable fuels using solid oxide electrolysis cells (SOECs): advanced materials and technology.* Chem Soc Rev, 2017. **46**(5): p. 1427-1463.

8. Lee, W.-H., et al., *A novel twin reactor for CO2 photoreduction to mimic artificial photosynthesis.* Applied Catalysis B: Environmental, 2013. **132**: p. 445-451.

9. Tu, W., Y. Zhou, and Z. Zou, *Photocatalytic conversion of CO2 into renewable hydrocarbon fuels: state‐of‐the‐art accomplishment, challenges, and prospects.* Advanced Materials, 2014. **26**(27): p. 4607-4626.

10. Le Gal, A., S. Abanades, and G. Flamant, *CO2 and H2O splitting for thermochemical production of solar fuels using nonstoichiometric ceria and ceria/zirconia solid solutions.* Energy & Fuels, 2011. **25**(10): p. 4836-4845.

11. Albo, J., et al., *Towards the electrochemical conversion of carbon dioxide into methanol.* Green Chemistry, 2015. **17**(4): p. 2304-2324.

12. Whipple, D.T. and P.J. Kenis, *Prospects of CO2 utilization via direct heterogeneous electrochemical reduction.* The Journal of Physical Chemistry Letters, 2010. **1**(24): p. 3451-3458.

13. Ebbesen, S.D., et al., *High temperature electrolysis in alkaline cells, solid proton conducting cells, and solid oxide cells.* Chem Rev, 2014. **114**(21): p. 10697-734.

14. Ebbesen, S.D. and M. Mogensen, *Electrolysis of carbon dioxide in Solid Oxide Electrolysis Cells.* Journal of Power Sources, 2009. **193**(1): p. 349-358.

15. Nernst, W., *On the electrolytic conduction of solid bodies at high temperatures.* Z. Electrochem, 1899. **6**(2): p. 41-43.

16. Möbius, H.-H., *On the history of solid electrolyte fuel cells.* Journal of solid state electrochemistry, 1997. **1**(1): p. 2-16.

17. Jacobson, A.J., *Materials for solid oxide fuel cells.* Chemistry of Materials, 2009. **22**(3): p. 660-674.

18. Irvine, J.T., et al., *Evolution of the electrochemical interface in high-temperature fuel cells and electrolysers.* Nature Energy, 2016. **1**(1): p. 15014.

19. Usseglio-Viretta, F., et al., *Quantitative microstructure characterization of a Ni–YSZ bi-layer coupled with simulated electrode polarisation.* Journal of Power Sources, 2014. **256**: p. 394-403.

20. Styring, P., E.A. Quadrelli, and K. Armstrong, *Carbon dioxide utilisation: closing the carbon cycle*. 2014: Elsevier.

21. Addo, P., et al., *CO/CO2 Study of High Performance La0. 3Sr0. 7Fe0. 7Cr0. 3O3–δ Reversible SOFC Electrodes.* Fuel Cells, 2015. **15**(5): p. 689-696.

22. Ruiz-Morales, J.C., et al., *Symmetric and reversible solid oxide fuel cells.* Rsc Advances, 2011. **1**(8): p. 1403-1414.

23. Tao, Y., et al., *Polarization properties of La0. 6Sr0. 4Co0. 2Fe0. 8O3-based double layer-type oxygen electrodes for reversible SOFCs.* Electrochimica Acta, 2009. **54**(12): p. 3309-3315.

24. Chiodelli, G. and L. Malavasi, *Electrochemical open circuit voltage (OCV) characterization of SOFC materials.* Ionics, 2013. **19**(8): p. 1135-1144.

25. O'hayre, R., et al., *Fuel cell fundamentals*. 2016: John Wiley & Sons.

26. Li, M., et al., *Carbon-tolerant Ni-based cermet anodes modified by proton conducting yttrium-and ytterbium-doped barium cerates for direct methane solid oxide fuel cells.* Journal of Materials Chemistry A, 2015. **3**(43): p. 21609-21617.

27. Bard, A.J. and L.R. Faulkner, *Fundamentals and applications.* Electrochemical Methods, 2001. **2**: p. 482.

28. Lay, E., G. Gauthier, and L. Dessemond, *Preliminary studies of the new Ce-doped La/Sr chromo-manganite series as potential SOFC anode or SOEC cathode materials.* Solid State Ionics, 2011. **189**(1): p. 91-99.

29. Tao, G., K. Sridhar, and C. Chan, *Study of carbon dioxide electrolysis at electrode/electrolyte interface: Part I. Pt/YSZ interface.* Solid State Ionics, 2004. **175**(1-4): p. 615-619.

30. Kan, W.H. and V. Thangadurai, *Challenges and prospects of anodes for solid oxide fuel cells (SOFCs).* Ionics, 2015. **21**(2): p. 301-318.

31. Yue, X. and J.T. Irvine, *Alternative cathode material for CO2 reduction by high temperature solid oxide electrolysis cells.* Journal of The Electrochemical Society, 2012. **159**(8): p. F442-F448.

32. Ni, M., M.K. Leung, and D.Y. Leung, *Technological development of hydrogen production by solid oxide electrolyzer cell (SOEC).* International Journal of Hydrogen Energy, 2008. **33**(9): p. 2337-2354.

33. Ishihara, T., N. Jirathiwathanakul, and H. Zhong, *Intermediate temperature solid oxide electrolysis cell using LaGaO 3 based perovskite electrolyte.* Energy & Environmental Science, 2010. **3**(5): p. 665-672.

34. Lakshmi, V.V., et al., *Synthesis and characterization of nanocrystalline ScSZ electrolyte for SOFCs.* International Journal of Hydrogen Energy, 2011. **36**(22): p. 14936-14942.

35. Zhu, B., et al., *Electrolysis studies based on ceria-based composites.* Electrochemistry communications, 2006. **8**(3): p. 495-498.

36. Bidrawn, F., et al., *Efficient reduction of CO2 in a solid oxide electrolyzer.* Electrochemical and Solid-State Letters, 2008. **11**(9): p. B167-B170.

37. Zhan, Z. and L. Zhao, *Electrochemical reduction of CO2 in solid oxide electrolysis cells.* Journal of Power Sources, 2010. **195**(21): p. 7250-7254.

38. Druce, J., et al., *Surface termination and subsurface restructuring of perovskite-based solid oxide electrode materials.* Energy & Environmental Science, 2014. **7**(11): p. 3593-3599.

39. Ye, L., et al., *Enhancing CO 2 electrolysis through synergistic control of non-stoichiometry and doping to tune cathode surface structures.* Nature communications, 2017. **8**: p. 14785.

40. Hauch, A., et al., *Ni/YSZ electrodes structures optimized for increased electrolysis performance and durability.* Solid State Ionics, 2016. **293**: p. 27-36.

41. Osada, N., H. Uchida, and M. Watanabe, *Polarization behavior of SDC cathode with highly dispersed Ni catalysts for solid oxide electrolysis cells.* Journal of the Electrochemical Society, 2006. **153**(5): p. A816-A820.

42. Tao, S. and J.T. Irvine, *A redox-stable efficient anode for solid-oxide fuel cells.* Nat Mater, 2003. **2**(5): p. 320-3.

43. Tao, S. and J.T. Irvine, *Synthesis and Characterization of (La0. 75Sr0. 25) Cr0. 5Mn0. 5 O 3− δ, a Redox-Stable, Efficient Perovskite Anode for SOFCs.* Journal of the electrochemical society, 2004. **151**(2): p. A252-A259.

44. Li, M., et al., *Charge transfer dynamics in RuO2/perovskite nanohybrid for enhanced electrocatalysis in solid oxide electrolyzers.* Nano Energy, 2019. **57**: p. 186-194.

45. Bo, Y., et al., *Microstructural characterization and electrochemical properties of Ba0. 5Sr0. 5Co0. 8Fe0. 2O3− δ and its application for anode of SOEC.* International journal of hydrogen energy, 2008. **33**(23): p. 6873-6877.

46. Zhang, Y.Q., et al., *Highly Active and Redox-Stable Ce-Doped LaSrCrFeO-Based Cathode Catalyst for CO2 SOECs.* ACS Appl Mater Interfaces, 2016. **8**(10): p. 6457-63.

47. Hua, B., et al., *Activating p-Blocking Centers in Perovskite for Efficient Water Splitting.* Chem, 2018. **4**(12): p. 2902-2916.

48. Sun, Y.-F., et al., *Electrochemical performance and carbon deposition resistance of Ce-doped La0. 7Sr0. 3Fe0. 5Cr0. 5O3-δ anode materials for solid oxide fuel cells fed with syngas.* Journal of Power Sources, 2015. **274**: p. 483-487.

49. Carter, S., et al., *Oxygen transport in selected nonstoichiometric perovskite-structure oxides.* Solid State Ionics, 1992. **53**: p. 597-605.

50. Liang, M., et al., *Preparation of LSM–YSZ composite powder for anode of solid oxide electrolysis cell and its activation mechanism.* Journal of Power Sources, 2009. **190**(2): p. 341-345.

51. Lee, S., et al., *Highly durable solid oxide fuel cells: suppressing chemical degradation via rational design of a diffusion-blocking layer.* Journal of Materials Chemistry A, 2018. **6**(31): p. 15083-15094.

52. Mai, A., et al., *Ferrite-based perovskites as cathode materials for anode-supported solid oxide fuel cells: Part II. Influence of the CGO interlayer.* Solid state ionics, 2006. **177**(19-25): p. 2103-2107.

53. Kim, S.J. and G.M. Choi, *Stability of LSCF electrode with GDC interlayer in YSZ-based solid oxide electrolysis cell.* Solid State Ionics, 2014. **262**: p. 303-306.

54. Lee, C.H. and G.M. Choi, *Electrical conductivity of CeO2-doped YSZ.* Solid State Ionics, 2000. **135**(1-4): p. 653-661.

55. Tsoga, A., et al., *Gadolinia-doped ceria and yttria stabilized zirconia interfaces: regarding their application for SOFC technology.* Acta Materialia, 2000. **48**(18-19): p. 4709-4714.

56. Anjaneya, K., et al., *Studies on structural, morphological and electrical properties of Ce0. 8Ln0. 2O2− δ (Ln= Y3+, Gd3+, Sm3+, Nd3+ and La3+) solid solutions prepared by citrate complexation method.* Journal of Alloys and Compounds, 2014. **585**: p. 594-601.

57. Hua, B., et al., *A coupling for success: Controlled growth of Co/CoO x nanoshoots on perovskite mesoporous nanofibres as high-performance trifunctional electrocatalysts in alkaline condition.* Nano Energy, 2017. **32**: p. 247-254.

58. Ding, D., et al., *Enhancing SOFC cathode performance by surface modification through infiltration.* Energy & Environmental Science, 2014. **7**(2): p. 552-575.

59. Van Dillen, A.J., et al., *Synthesis of supported catalysts by impregnation and drying using aqueous chelated metal complexes.* Journal of Catalysis, 2003. **216**(1-2): p. 257-264.

60. Jiang, S.P., *Nanoscale and nano-structured electrodes of solid oxide fuel cells by infiltration: advances and challenges.* International journal of hydrogen energy, 2012. **37**(1): p. 449-470.

61. Sun, Y., et al., *A-site deficient perovskite: the parent for in situ exsolution of highly active, regenerable nano-particles as SOFC anodes.* Journal of Materials Chemistry A, 2015. **3**(20): p. 11048-11056.

62. Hua, B., et al., *Enhancing Perovskite Electrocatalysis of Solid Oxide Cells Through Controlled Exsolution of Nanoparticles.* ChemSusChem, 2017. **10**(17): p. 3333-3341.

63. Sun, Y.F., et al., *New Opportunity for in Situ Exsolution of Metallic Nanoparticles on Perovskite Parent.* Nano Lett, 2016. **16**(8): p. 5303-9.

64. Neagu, D., et al., *In situ growth of nanoparticles through control of non-stoichiometry.* Nature chemistry, 2013. **5**(11): p. 916.

65. Hicks, J.C., et al., *Designing adsorbents for CO2 capture from flue gas-hyperbranched aminosilicas capable of capturing CO2 reversibly.* Journal of the American Chemical Society, 2008. **130**(10): p. 2902-2903.

66. Ding, D., et al., *Enhancing SOFC cathode performance by surface modification through infiltration.* Energy & Environmental Science, 2014. **7**(2).

67. Li, M., et al., *Thermally stable and coking resistant CoMo alloy-based catalysts as fuel electrodes for solid oxide electrochemical cells.* Journal of Materials Chemistry A, 2018. **6**(31): p. 15377-15385.

68. Hua, B., et al., *Anode-Engineered Protonic Ceramic Fuel Cell with Excellent Performance and Fuel Compatibility.* Adv Mater, 2016. **28**(40): p. 8922-8926.

69. Kresse, G. and J. Furthmüller, *Efficient iterative schemes for ab initio total-energy calculations using a plane-wave basis set.* Physical review B, 1996. **54**(16): p. 11169.

70. Kresse, G. and J. Furthmüller, *Efficiency of ab-initio total energy calculations for metals and semiconductors using a plane-wave basis set.* Computational materials science, 1996. **6**(1): p. 15-50.

71. Chick, L.A., et al., *Glycine-nitrate combustion synthesis of oxide ceramic powders.* Materials letters, 1990. **10**(1-2): p. 6-12.

72. Pennycook, S.J. and P.D. Nellist, *Scanning transmission electron microscopy: imaging and analysis*. 2011: Springer Science & Business Media.

73. Danilovic, N., et al., *Correlation of fuel cell anode electrocatalytic and ex situ catalytic activity of perovskites La0. 75Sr0. 25Cr0. 5X0. 5O3− δ (X= Ti, Mn, Fe, Co).* Chemistry of Materials, 2009. **22**(3): p. 957-965.

74. Wei, T., et al., *A high power density solid oxide fuel cell based on nano-structured La 0.8 Sr 0.2 Cr 0.5 Fe 0.5 O 3-δ anode.* Electrochimica Acta, 2014. **148**: p. 33-38.

75. Jiang, S.P., *A review of wet impregnation—an alternative method for the fabrication of high performance and nano-structured electrodes of solid oxide fuel cells.* Materials Science and Engineering: A, 2006. **418**(1-2): p. 199-210.

76. Hansen, H.A., et al., *Understanding Trends in the Electrocatalytic Activity of Metals and Enzymes for CO2 Reduction to CO.* J Phys Chem Lett, 2013. **4**(3): p. 388-92.

77. Foit, S.R., et al., *Power-to-Syngas: An Enabling Technology for the Transition of the Energy System?* Angew Chem Int Ed Engl, 2017. **56**(20): p. 5402-5411.

78. Pan, Z., et al., *Effect of La0. 6Sr0. 4Co0. 2Fe0. 8O3− δ air electrode–electrolyte interface on the short-term stability under high-current electrolysis in solid oxide electrolyzer cells.* Journal of Power Sources, 2018. **378**: p. 571-578.

79. Tietz, F., et al., *Degradation phenomena in a solid oxide electrolysis cell after 9000 h of operation.* Journal of Power Sources, 2013. **223**: p. 129-135.

80. Neagu, D., et al., *Nano-socketed nickel particles with enhanced coking resistance grown in situ by redox exsolution.* Nature communications, 2015. **6**: p. 8120.

81. Du, Z., et al., *High-Performance Anode Material Sr2FeMo0.65Ni0.35O6-delta with In Situ Exsolved Nanoparticle Catalyst.* ACS Nano, 2016. **10**(9): p. 8660-9.

82. Neagu, D., et al., *Nano-socketed nickel particles with enhanced coking resistance grown in situ by redox exsolution.* Nat Commun, 2015. **6**: p. 8120.

83. Hua, B., et al., *Novel layered solid oxide fuel cells with multiple-twinned Ni0.8Co0.2 nanoparticles: the key to thermally independent CO2 utilization and power-chemical cogeneration.* Energy & Environmental Science, 2016. **9**(1): p. 207-215.

84. Hamada, I., et al., *A Density Functional Theory Study of Self-Regenerating Catalysts LaFe1–x M x O3–y (M= Pd, Rh, Pt).* Journal of the American Chemical Society, 2011. **133**(46): p. 18506-18509.

85. Zhang, J., et al., *Composite titanate cathode enhanced with in situ grown nickel nanocatalyst for direct steam electrolysis.* New Journal of Chemistry, 2014. **38**(8).

86. Kim, K.J., et al., *A Highly Active and Redox-Stable SrGdNi0.2Mn0.8O4±δ Anode with in Situ Exsolution of Nanocatalysts.* ACS Catalysis, 2019: p. 1172-1182.

87. Kwon, O., et al., *Exsolution trends and co-segregation aspects of self-grown catalyst nanoparticles in perovskites.* Nature communications, 2017. **8**: p. 15967.

88. Perdew, J.P., K. Burke, and M. Ernzerhof, *Generalized gradient approximation made simple.* Physical review letters, 1996. **77**(18): p. 3865.

89. Monkhorst, H.J. and J.D. Pack, *Special points for Brillouin-zone integrations.* Physical review B, 1976. **13**(12): p. 5188.

90. Kirklin, S., et al., *The Open Quantum Materials Database (OQMD): assessing the accuracy of DFT formation energies.* npj Computational Materials, 2015. **1**: p. 15010.

91. Ye, L., et al., *Enhancing CO2 electrolysis through synergistic control of non-stoichiometry and doping to tune cathode surface structures.* Nat Commun, 2017. **8**: p. 14785.

92. Yue, X. and J.T. Irvine, *Impedance studies on LSCM/GDC cathode for high temperature CO2 electrolysis.* Electrochemical and solid-state letters, 2012. **15**(3): p. B31-B34.

93. Tao, S. and J.T. Irvine, *Catalytic properties of the perovskite oxide La0. 75Sr0. 25Cr0. 5Fe0. 5O3-δ in relation to its potential as a solid oxide fuel cell anode material.* Chemistry of materials, 2004. **16**(21): p. 4116-4121.